

ISTANBUL TECHNICAL UNIVERSITY ★ GRADUATE SCHOOL OF SCIENCE
ENGINEERING AND TECHNOLOGY

**FREQUENCY-DEPENDENT SHEAR WAVE ATTENUATION ALONG THE
WESTERN PART OF THE NORTH ANATOLIAN FAULT ZONE, TURKEY**



M.Sc. THESIS

Gizem İZGİ

Department of Geophysical Engineering

Geophysical Engineering Programme

DECEMBER 2018

ISTANBUL TECHNICAL UNIVERSITY ★ GRADUATE SCHOOL OF SCIENCE
ENGINEERING AND TECHNOLOGY

**FREQUENCY-DEPENDENT SHEAR WAVE ATTENUATION ALONG THE
WESTERN PART OF THE NORTH ANATOLIAN FAULT ZONE, TURKEY**



M.Sc. THESIS

Gizem İZGİ
(505161419)

Department of Geophysical Engineering

Geophysical Engineering Programme

Thesis Advisor: Dr. Tuna EKEN

DECEMBER 2018

İSTANBUL TEKNİK ÜNİVERSİTESİ ★ FEN BİLİMLERİ ENSTİTÜSÜ

**KUZEY ANADOLU FAYININ BATISINDA, FREKANS BAĞLI
S-DALGALARININ SÖNÜMLENMESİ**

YÜKSEK LİSANS TEZİ

**Gizem İZGİ
(505161419)**

Jeofizik Mühendisliği Anabilim Dalı

Jeofizik Mühendisliği Programı

Tez Danışmanı: Dr. Tuna EKEN

ARALIK 2018

Gizem İzgi, a M.Sc. student of ITU Graduate School of Science Engineering and Technology student ID 505161419, successfully defended the thesis entitled “FREQUENCY-DEPENDENT SHEAR WAVE ATTENUATION ALONG THE WESTERN PART OF THE NORTH ANATOLIAN FAULT ZONE, TURKEY”, which she prepared after fulfilling the requirements specified in the associated legislations, before the jury whose signatures are below.

Thesis Advisor : **Dr. Tuna EKEN**
Istanbul Technical University

Jury Members : **Prof. Dr. Tuncay TAYMAZ**
Istanbul Technical University

Prof. Dr. Ali PINAR
Boğaziçi University

Dr. Tuna EKEN
Istanbul Technical University

Date of Submission : 16 November 2018
Date of Defense : 14 December 2018





To my beloved family and KevKevilla,



FOREWORD

First and foremost I would like to express my gratitude to my thesis advisor Dr. Tuna Eken for his guidance on scientific matters as well as for his helps when I struggle with technical difficulties when preparing this thesis project.

Qopen utilities designed using Python language was for forward and inverse modelling of coda waves. Hence, I would like to express my sincere gratitudes mainly to Dr. Peter J. Gaebler of the BGR-Hannover for his valuable co-operation and technical support regarding the usage of Qopen utilities and Dr. Tom Eulenfeld of the University of Jena for his comments on the findings of this thesis.

I would like to deliver my special thanks for Prof. Dr. Tuncay Taymaz for his wisdom, generosity and creating warm environment in the Seismology Lab. I also thank Assoc. Prof. Dr. Seda Yolsal Çevikbilen for her kind attitude.

The facilities of IRIS Data Services, and specifically the IRIS Data Management Center, were used for access to waveforms, related metadata, and/or derived products used in this study. IRIS Data Services are funded through the Seismological Facilities for the Advancement of Geoscience and EarthScope (SAGE) Proposal of the National Science Foundation under Cooperative Agreement EAR-1261681. Data for the DANA experiment (https://doi.org/10.7914/SN/YH_2012) are available from the IRIS Data Management Center at <http://www.iris.edu/hq/>.

The Qopen python code used for carrying out the inverse modeling is available under the permissive MIT license and is distributed at <https://github.com/trichter/qopen>. We are grateful to the IRIS Data Management Center for maintaining, archiving and making the continuous broadband data used in this study open to the international scientific community.

Last but not the least, thanks everybody who were with me at this journey.

December 2018

Gizem İzgi



TABLE OF CONTENTS

	<u>Page</u>
FOREWORD	ix
TABLE OF CONTENTS	xi
ABBREVIATIONS	xiii
SYMBOLS	xv
LIST OF TABLES	xvii
LIST OF FIGURES	xix
SUMMARY	xxi
ÖZET	xxiii
1. INTRODUCTION	1
1.1 Content and Purpose of Thesis.....	2
1.2 Study Area.....	3
1.2.1 Tectonic setting.....	3
1.2.2 Geological overview	4
1.3 Early Studies	5
1.4 . Seismic Coda Waves.....	8
1.4.1 Scattering energy	9
1.4.2 Coda excitation models.....	10
1.4.2.1 Single back-scattering model.....	10
1.4.2.2 Diffusion model	11
1.4.2.3 Energy-flux model	12
1.4.2.4 Radiative transfer theory.....	13
1.4.3 Historical background on coda wave approaches.....	16
2. DATA	19
3. METHODOLOGY	23
3.1. General Remarks	23
3.2. Separation of Intrinsic and Scattering Attenuation	23
3.3. Calculation of Observed Densities	24
4. INVERSION	25
4.1. Estimation of Attenuation Parameters.....	25
4.2. Estimation of Source Parameters	27
5. RESULTS AND INTERPRETATIONS	31
5.1. Structural Parameters	31
5.1.1. 2D lateral variations of attenuation.....	31
5.1.2. Comparison among different tectonic units	34
5.2. Magnitude Estimates	36
6. CONCLUSION	39
REFERENCES	41
CURRICULUM VITAE	51



ABBREVIATIONS

CNM	: Coda Normalization Method
DANA	: Dense Array of North Anatolia
DSF	: Dead Sea Fault
EAFZ	: East Anatolian Fault Zone
GM	: Geometric Mean
KB	: Kuzuluk Basin
MLTWA	: Multiple Lapse Time Window Analysis
NAFZ	: North Anatolian Fault Zone
PGV	: Peak Ground Velocity
RTE	: Radiative Transfer Equations
RTT	: Radiative Transfer Theory



SYMBOLS

A	: Rupture Area
A₀	: Amplitude of a Reference Event
A_{max}	: Maximum Ground Amplitude
a(n, x)	: Angularly Resolved Energy Density
b	: Absorption Parameter
C	: Constant
D	: Diffusivity
δs	: Path Element
ε	: Misfit Function
E_{mod}	: Modelled Energy Density
E_{obs}	: Observed Energy Density
F	: Green's Function of Coherent Wave Energy
f_c	: Corner Frequency
g*	: Transient Scattering Coefficient
g₀	: Scattering Coefficient
g	: Fixed Scattering Coefficient
G	: Green's Function
H	: Heaviside Step Function
ℋ	: Hilbert Transfer
I	: Specific Intensity
J	: Energy Flux Density
M_l	: Local Magnitude
M_w	: Moment Magnitude
M₀	: Seismic Moment
N_E	: Observed Energy Densities of Events with Index j
N_s	: Observed Energy Densities of Stations with Index i
N_{ij}	: Observed Energy Densities of Every Events in Each Station with Index k
n	: Incident Direction
n	: High Frequency Fall-off

$Q(\Delta, h)$: Distance and Depth Dependent Factor
Q_i	: Intrinsic Quality Factor
Q_s	: Scattering Quality Factor
Q_c	: Coda
R	: Site Amplification Factor
$r^2 d\Omega$: Surface Element
r	: Distance
t	: Time
$\langle \dot{u}^2 \rangle$: Mean Square Velocity
u	: Average Fault Displacement
V_0	: Average Velocity for S-waves
V_s	: S-wave Velocity
V_p	: P-wave Velocity
v	: Velocity Element
W	: Spectral Source Energy
ω	: Angular velocity
$\omega M(f)$: Source Displacement Spectrum
ρ_0	: Mean Mass Density
ρ	: Rock Density
Δ	: Epicentral Distance
Ω_0	: Spectral Level of Long Period S waves
γ	: Sharpness
μ	: Rigidity

LIST OF TABLES

	<u>Page</u>
Table 5.1: Minimum and maximum calculated values of Q_i^{-1} , Q_s^{-1} , Q_t^{-1} at five different frequency bands	32
Table 5.2: Best-fitting power laws for total attenuation Q_t^{-1} as a function of frequency.....	34





LIST OF FIGURES

	<u>Page</u>
Figure 1.1. : (a) Tectonic settings of Anatolia and surrounding regions. Major shear zones shown in red (NAF: North Anatolian Fault, EAF: East Anatolian Fault, DSF: Dead Sea Fault) Yellow rectangle represents study region (b) Tectonic boundaries shown in yellow, NAFZ in red and black framed white stars are İzmit and Düzce Earthquakes. KB: Kuzuluk Basin. Black triangles are 71 broadband stations of DANA network.....	5
Figure 1.2. : A waveform example shows direct P- and S-waves, coda portion of the seismogram and the coda envelope (Okamoto et al., 2013).....	9
Figure 1.3. : Illustration of scattering energy representation from a scatterer (Sato et al., 2012).....	9
Figure 1.4. : Simple illustration of single back-scattering model for a common source and receiver location. Distance between the source and scatterer represented as r	11
Figure 1.5. : Illustration of energy flux model. (a) time traces at different scaled distances (b) spatial distribution of normalized energy. The shaded area represents the direct wave energy density (Sato et al., 2012).....	12
Figure 1.6. : Energy flux in RTT. Energy is emitted from the emitting surface (ES) through the receiving surface (RS) around a direction of \mathbf{n} . In addition to this pattern, some portions of the energy are reduced by scattering through other directions (A), dissipation (B) but flux can increase by scattering from other directions gathers into the direction \mathbf{n} (C) and scatterers from another sources along the path (D) (Gaebler, 2015).....	14
Figure 2.1. : Visually selected 3-component waveform example in our dataset.....	20
Figure 2.2. : (a) 1035 earthquakes (circles) with three different colored ray paths according to their position relative to the NAFZ strands (red). 71 stations are given as black triangles. (b) 249 earthquakes (circles) coloured by their magnitudes. 71 stations are given as white triangles.....	21
Figure 4.1. : Optimization with error function is given for one event (20120707070746) observed in 22 stations in 8-16 Hz frequency band. The big panel refers to the optimization and blue cross is the point where $g^* = g_0$. Remaining small panels, the least square solutions are represented in 6 guesses and one best solution in lower right-hand sided	

panel where grey curves and dots are the observed envelopes of coda and direct S-wave. The best guess represents the best value of g_0 with low misfit.....27

Figure 4.2. Example fits between observed and modeled envelopes for a specific event (red star on the map) recorded at four stations (black triangles on the map) are shown for five frequency bands. Observed raw and smoothed envelopes are represented by grey and blue color, respectively. Red decaying curve indicates synthetic envelope computed for optimal parameters reached at the end of inversion process.....28

Figure 4.3. : Illustration of inversion for source parameters of an earthquake (20120707070746)..... 30

Figure 5.1. : 2-D variation of the inverse of the quality factors (Q_i^{-1} , Q_s^{-1} , Q_t^{-1}) that represent seismic intrinsic (left), scattering (middle) and total attenuation (right) parameters in the study area for investigated frequency bands (increasing from top to bottom). Blueish colors mean weaker attenuation while reddish colors indicate stronger attenuation. Triangles show the station location and color coded by the corresponding attenuation values. Attenuation values between stations are interpolated.....33

Figure 5.2. : Inverse of the quality factors (Q_i^{-1} , Q_s^{-1} , Q_t^{-1}) that vary with frequency in the northern (blue), southern (red) and middle (yellow) region of the western part of the NAFZ.....34

Figure 5.3. : Comparison between catalog magnitudes of local events with those derived from coda waves as a side product of the inversion process.....37

FREQUENCY-DEPENDENT SHEAR WAVE ATTENUATION ALONG THE WESTERN PART OF THE NORTH ANATOLIAN FAULT ZONE

SUMMARY

Active tectonics and deformation of Anatolian plate are driven by the northward convergence of African and Arabian plates to Eurasian plate. This type of movement, has resulted in the development of two major shear zones occurred, namely, East Anatolian Fault Zone (EAFZ) and North Anatolian Fault Zone (NAFZ) and a westward escape of Anatolia along these shear deformation zones. The NAFZ, a transform boundary between Eurasian and Anatolian plates with a length of about 1600 km, is one of the most prominent tectonic features in Turkey and has been attracting an extensive focus in scientific community due to its seismic hazard potential for a large area including the mega-city Istanbul. This thesis focuses on seismic attenuation properties within the crustal part of the western NAFZ which separated into two branches resulting in Istanbul-Zonguldak, Armutlu-Almacık and Sakarya Zones.

A proper knowledge of the crustal structure along the NAFZ, plays a key role in understanding the past/present tectonic processes in relation to the deformation history. Hence the main motivation of this thesis is to investigate crustal heterogeneities along seismically most active part at present which is the western part of the NAFZ by investigating the attenuation properties. Seismic attenuation can provide hints about ductile and/or brittle type of deformation characteristics of a region that would be observed by the seismic waves amplitude. During the wave propagation from source to receiver, the amplitude of seismic waves decreases due to the intrinsic and scattering attenuation properties of a heterogeneous medium.

Aim of this study is to reveal 2D lateral distribution of frequency-dependent crustal attenuation parameters along the western part of NAFZ. To compute synthetic seismograms, an approach that is based on acoustic radiative transfer theory (RTT) and allows the separation of intrinsic and scattering attenuation, under the assumption of multiple isotropic scattering was employed. In the next step, the estimation of intrinsic and scattering attenuation parameters was achieved applying an inversion procedure that depends on finding an optimal fit between synthetically computed and observed seismogram envelopes in five different frequency bands (0.75 to 12 Hz). The successful fits between synthetically computed envelopes and the observed envelopes confirmed that our approach could be even applied in a study area with this tectonically active and complex regime.

In this study, we used local seismic activity recorded at seismic stations of a temporary passive seismic network, the Dense Array of North Anatolia (DANA), that was operated between 2012 and 2013. Three component waveforms of the dataset from 1315 events recorded on 71 broadband stations within the array were extracted. We selected local earthquakes with magnitudes between 0.1 to 4.1, station-event pair distances less than 120 km, and focal depths less than 10 km. The second criteria is to avoid Moho boundary guided Sn-waves while third one allows us to focus on upper crustal region.

Main outcome of this thesis is the 2D lateral variation of intrinsic and scattering attenuation at various frequencies in relation to the presence of major tectonic zones, i.e., Armutlu-Almacık, Istanbul-Zonguldak and Sakarya Zones that are separated by the Southern and Northern branches of the western part of the NAFZ and the depth extensions of these zones. Our findings clearly evidence these zones represented by significant lithological contrasts.

Overall, scattering attenuation appears to be dominant over intrinsic attenuation in the study area at relatively low frequencies (0.75, 1.5, and 3 Hz) while intrinsic attenuation controls the attenuating behavior at higher frequencies (6 and 12 Hz). Beneath the older Istanbul Zone we observe relatively low attenuation properties while the values for younger Sakarya Zone is relatively high. This contrast shows that the method explicitly indicates the significance of present lithological conditions. Furthermore, the Armutlu-Almacık block shows more complex and laterally varying attenuation properties which is found to be coherent with early geophysical findings observed for the area. In particular, attenuation properties over Kuzuluk Basin which is a pull-apart basin formed due to west-east extensional deformation are characterised by very high values.

In addition to the attenuation parameters, as a side product of this thesis we provide coda-derived magnitudes. Since our approach yields source displacement spectrum we were able to calculate the moment magnitudes (M_w) for each earthquake and they represent a good correlation with catalog magnitudes which implies that our non-empirical inversion approach is successful.

KUZEY ANADOLU FAYININ BATISINDA, FREKANS BAĞLI S-DALGALARININ SÖNÜMLENMESİ

ÖZET

Anadolu plakasının aktif tektonizması ve deformasyonu başlıca Arap ve Afrika plakalarının Avrasya plakasına doğru hareketinden kaynaklanır. Bu hareketin sonucunda, Anadolu plakası batıya doğru itilmesiyle bir kaçış hareketi gerçekleştirir ve Türkiye’de bulunan iki büyük makaslama zonu oluşur: Doğu Anadolu Fay Zonu (DAFZ) ve Kuzey Anadolu Fay Zonu (KAFZ). KAFZ Avrasya ve Anadolu plakalarının arasında bulunan yaklaşık 1600 km’lik bir transform fay hattıdır. Türkiye’nin en önemli tektonik özelliği olup, bilim insanları tarafından yıllardır özenle incelenmektedir. KAFZ’ye olan bu ilginin sebebi ise 1939 yılında fay hattının doğusunda Erzincan depremiyle başlayarak son olarak 1999 yılında Düzce (Mw=7.2) ve İzmit (Mw=7.4) illerinde meydana gelmiş büyük depremler serisinin batıya doğru hareketinin gözlemlenmesidir. Aynı zamanda Türkiye’nin büyük şehirlerinden biri olan İstanbul’un KAFZ’nin batı kısmında konumlanmış olması ve beklenen bir sonraki yıkıcı depremin İstanbul’a etkilerinin büyük hasarlara yol verebileceği düşünülmektedir. Bu tezin içeriği ise KAFZ’nin batı kısmındaki kabukta sismik sönümlenme özelliklerinin incelenmesidir. Çalışma alanında KAFZ’nin iki ayrı kola (kuzey kolu ve güney kolu) ayrılmasıyla İstanbul-Zonguldak, Armutlu-Almacık ve Sakarya zonları gözlemlenir.

KAFZ boyunca kabuk yapısının iyi anlaşılması şimdiki ve geçmişteki tektonik aktivitelerin anlaşılmasında önemli bir yer arz eder. Bu sebeple, bu tezin amacı şuanda KAFZ’nin sismik anlamda en aktif olan batı bölgesindeki kabuk yapısını sönümlenme parametreleriyle detaylı bir biçimde incelemektir. Sismik sönümlenme, deformasyonun biçimiyle ilgili ayrıntılı bilgi sağlamaktadır. Süneklik ve kırılma kavramları sönümlenme şekilleriyle incelenebilmektedir. Örneğin saçılmadan kaynaklı sönümlenme ufak dağıtıcıların çokluğundan kaynaklı daha kırılma bir yapı göstermektedir. Oysaki içsel sönümlenmenin baskınlığı muhtemel bir ısı kaynağını işaret ederek sünek deformasyonu işaret eder.

Bu çalışmanın amacı KAFZ’nin batı kısmındaki sönümlenme parametrelerinin iki boyutlu olarak çizdirilerek, bölgedeki kabuk deformasyonunu detaylı olarak incelemektir. Bu amaç doğrultusunda sentetik sismogramlar akustik radiatif transfer teorisiyle (RTT) çoklu eşyönlü saçılmalar yaklaşımıyla oluşturulmuştur. RTT kullanarak sönümlenme tipi ayrıştırılmıştır. Bu yaklaşımda gözlemlenen sismik dalganın kuyruk kısmıyla oluşturulan sismik dalga zarfı direk olarak birbirine oturtulur. Bu yöntemde kuyruk düzeltilmesi yapılmamasına rağmen, yön bağımlı saçılmalar için de geçerlidir. Kullanılan ters çözüm yöntemi ise beş farklı frekans bandında (0.75’ten 12 Hz’e kadar) en iyi kuyruk çakışmasını sağlamayı amaçlar. Gözlemlenen sismik dalganın kuyruk zarfının sentetik olarak oluşturulan zarfla tam olarak örtüşmesi, yöntemin tektonik anlamda bu kadar karmaşık ve aktif bir alanda bile doğru çalıştığına göstergesidir.

Bu çalışmada Dense Array of North Anatolia (DANA) adlı çalışma ile toplanan lokal sismik aktivite kullanılmıştır. Bu geçici sismik ağ 2012 ile 2013 yılları arasında durmaksızın veri toplamıştır. Üç bileşenli dalga-biçimleri bu ağa bağlı çalışan 7

kilometre aralıkla dizilmiş, 71 istasyondan gelen 1315 işlenmemiş deprem verisinden çıkarılmıştır. Lokal magnitüdler 0.1 ile 4.1 arasında değişmektedir. İstasyon ile deprem arasındaki mesafe maksimum 120 km olarak seçilmiştir. Bunun sebebi Moho sınırından yansıyan Sn dalgalarından korunmaktır. Aynı zamanda alt kabuk ve üst mantonun etkilerinden kurtulmak amacıyla odak derinlikleri maksimum 10 km olan depremler alınmıştır. Bu kısıtları koyduktan sonra elimizde 1035 deprem kalmış olmakla birlikte, ters çözümün doğru çalıştığını garantilemek adına bazı parametreler seçilmiştir. Örneğin kuyruk penceresi 10 saniyeden kısa olan depremler için ters çözüm çalışmaz, S-dalgası enerjisinin tamamını yakalamak amacıyla, kesme dalgası penceresi S-dalgasının varışından üç saniye önce başlar ve varıştan 7 saniye sonrasında biter. Sinyal bölü gürültü oranının 2.5 in altına düştüğü durumlarda ters çözüm o depremi atlar ve kuyruk penceresi en fazla 100 saniye olarak ayarlanmıştır. Bütün bu seçim parametrelerinin sonucunda 249 deprem kalmıştır. Deprem sayısının kayda değer şekilde azalması, ters çözüm kalitesinin ve tutarlılığının artışıyla birlikte problem olarak görülmemiştir.

Kuyruk dalgaları geçmişten bu yana bir çok çalışmada kullanılmıştır. Yapılan çalışmalar sonucu, sismogramın, sönümlenmenin ve saçılımın en iyi gözlemlendiği kısmı olarak kabul edilmişlerdir. Bu nedenle bu çalışmada kuyruk dalgaları kullanılmıştır. Bu çalışmadaki amaç sönümlenmenin kaynağını açığa çıkarmak ve buna bağlı bir harita elde etmek olduğundan kuyruk dalgası içeriğinden bu parametreleri ayırdık. Saçılmadan kaynaklı sönümlenme ve esas enerji dönüşümünden kaynaklı sönümlenmeyi ayırarak bölgenin kabuk yapısını incelemiş olduk. İki farklı sönümlenme türünden elde edilen sonuçları, bölgede önceden yapılmış jeofizik ve jeolojik çalışmalar ile birarada inceleyerek ters çözüm yönteminin bu koşullar altında doğru işlediğinden emin olduk.

Bu tezin sonuçlarından bir tanesi sönümlenmelerin beş farklı frekans bandında iki boyutlu yanal değişim haritalarıdır. Oluşturulan haritalar KAFZ'nin batısındaki farklı litolojilere sahip üç ayrı zonu göstermektedir. Armutlu-Almacık, İstanbul-Zonguldak ve Sakarya zonları bu alanda KAFZ'nin kuzey ve güney kolları ile birbirinden ayrılmaktadır. Yöntem sonucunda bu kolların ayırdığı üç ayrı zonu haritalandırarak yöntemin gerektiği gibi işlediğinden emin olduk.

Genel olarak sonuçlarda, saçılmalarından kaynaklı sönümlenme, düşük frekanslarda (0.75, 1.5, 3.0 Hz) baskın olarak gözlemlenmiştir. Bunun yanı sıra, yüksek frekanslarda (6.0, 12.0 Hz) ise baskınlığını kaybederek yerini içsel sönümlenmeye bırakmıştır. Bu da sığ alanlarda içsel sönümlenmenin derin alanlarda ise saçılmalarından kaynaklı sönümlenmenin baskın olduğuna işaret eder. Daha yaşlı ve sağlam olan İstanbul-Zonguldak zonunda daha düşük sönümlenme, daha genç Sakarya zonunda ise daha yüksek sönümlenme değerleri gözlemlenmiştir. Bu fark, çalışmanın amacına yönelik uygun sonuçlar verdiğinin kanıtıdır. Bu iki farklı litolojik birimin farklı sismik özellikler gösterdiği önceden yapılan çalışmalarda da gösterilmiştir. Aynı zamanda bu iki birimden parçalar barındıran orta segment derinliğe bağlı olarak değişen sönümlenme değerleriyle tekrardan ispatlanmıştır. Ayrıca alanda yapılmış diğer çalışmaların da belirttiği gibi Armutlu-Almacık zonu karmaşık ve heterojen bir yapıya sahiptir ve bu yapı nedeniyle sönümlenme değerleri bu zon içinde değişiklik göstermektedir. Daha ayrıntılı bahsetmek gerekirse, bu zonda batı-doğu açılmasından kaynaklı oluşmuş Kuzuluk baseni çok yüksek sönümlenme değerlerine sahiptir. Dolayısıyla yöntem, önceki çalışmalarda sismik hız anlamında düşük değerler vermiş olan Kuzuluk baseninde beklenen çok yüksek sönümlenme değerlerini göstermeyi başarmıştır. Genel olarak çalışmanın sonuçları, alanda yapılmış diğer jeofizik ve jeoloji araştırmalarına uyumlu sonuçlar göstermiştir.

Ayrıca sismologlar tarafından önem arz eden bir diğer bilgi ise depremin büyüklüğüdür. Bu büyüklük yıllar boyunca farklı şekillerde ifade edilmiştir. Ancak büyüklüğü en iyi tasfir eden moment magnitudüdür. Bu büyüklük çeşidi aynı zamanda diğer büyüklükler arasında bir geçiş sağlar. Bu nedenle bu çalışmada, ters çözüm esnasında her bir depremin lokal magnitudünden moment magnitudüne geçilmiştir. Yöntem bu noktada sismogramda var olan kaynak enerjisini fourier dönüşümünü kullanarak kaynak spektrumuna çevirir. Bu sayede sismik momentin hesaplanabileceği bir denklem oluşturulmuş olur. Sonrasında ise sismik momentten moment magnitudüne geçiş denklemleri kullanılarak her bir depremin moment magnitudü hesaplanmış olur.

Bütün bunların yanında, bu çalışmanın yan ürünü ise magnitud hesabıdır. Her bir deprem için hesaplanan moment magnitudleri, çalışma sırasında kullanılan depremlerin lokal magnitudlerle uyumlu olduğu gözlemlenmiştir ki bu da deneysel yaklaşımla yapılmamış olan ters çözüm yöntemimizin başarılı çalıştığını kanıtlar niteliktedir.





1. INTRODUCTION

An earthquake can be considered as the vibration of the ground that is caused by the sudden release of elastic energy stored in rocks. Released elastic energy propagates outward from the source as seismic waves. Seismology investigates various earthquakes as natural source of information to understand the behavior of ad resultant seismic waves propagation with respect to the stress changes within the Earth. During last few decades, increasing amount of seismic stations and available datasets have enourmously helped seismologists revealing the unknowns of the Earth and highlight the inner structure in detail. Today, in seismology, there are many efforts to model physical properties of crustal structure (e.g. seismic velocity, attenuation, et.), which is vitally important for the studies of seismic hazard mitigation, focal mechanism solutions and strain localizations.

Following Aki (1969) and Aki & Chouet (1975), coda parts of the seismograms that emerge due to the randomly distributed in lithosphere have become popular among seismologists. Coda wave analyses, in particular, are preferred when estimating small scale heterogenities and relative attenuation parameters due to scattering and absorption. Deterministic approaches are considered to be inadequate when investigating influences of heterogenities on seismic wave propagation.

In this study, we used frequency dependent shear wave attenuation properties to estimate the crustal structure beneath the western part of NAFZ which has complex and active regime. Seismic attenuation is closely related with seismic velocity properties at a given region. Seperation of intrinsic attenuation from scattering attenuation could be useful in elucidating the type of deformation. For instance, dominance of absorption over scattering may indicate ductile deformation due to the presence of a heat source while the dominance of scattering attenuation could be more related to small scale heterogenities within upper crust where the brittle deformation is prevalent.

Several approaches exist to calculate the attenuation parameters. Current work depends on using a non-empirical modeling approach, which allows to determine intrinsic and scattering attenuation parameters simultaneously. It employs the acoustic

RTT for the forward modelling of coda waves under the assumption of multiple isotropic scattering. We adapted a python-based software utilities called as called *Qopen* to our local earthquake dataset.

1.1 Content and Purpose of Thesis

Seismic attenuation is a complex phenomenon that corresponds to the energy loss of seismic waves while propagating from source to any direction and controlled by several conditions over propagation path. There are mainly three factors that cause loss of seismic energy. First one is geometrical spreading that leads to energy loss due to the energy of spherical wavefront emanating from a point source and distributed over a spherical surface with increasing size. In this case, seismic wave amplitude and energy decreases inversly proportional with the distance from the source (r) and its square. Second quantity is intrinsic attenuation, which results from the conversion of energy into other forms (e.g. shear heating at grain boundaries, mineral dislocations) since the waves do not propogate with complete elasticity. In addition to these two, seismic waves lose energy due to scattering at small scale heterogenities and this can lead to an exponential decay in amplitude (Aki, 1969; Aki and Chouet, 1975).

Investigation of seismic attenuation parameters within the upper crustal structure of the western part of the NAFZ is within the scope of this thesis work. Knowledge of crustal structure properties a type of deformation is crucial to make proper assesment of seismic hazard potential for study area that has experienced several large earthquakes. In this thesis, we focused on S-wave attenuation specifically because, usually S-waves produce higher peak ground velocity (PGV), which makes them preferred for seismic hazard analyses rather than P-waves. Furthermore, seismic attenuation provides accurate information about the type of deformation whether ductile or brittle which affects the characteristics of seismic wave amplitudes (e.g. Weber et al., 2004; Wilson et al., 2004). Using coda waves as a tool to investigate source parameters is considered to be more advantageous compared to direct waves since coda waves are not effected by source radiation pattern effects sphere (e.g. Aki, 1969; Aki and Chouet, 1975; Mayeda and Walter, 1996; Eken et al., 2004; Gök et al., 2016; Pasyanos et al., 2016). Coda wave analyses resulted in moment magnitude estimates of the analyzed earthquakes as a bi-product of the inversion process.

1.2 Study Area

Understanding the transient mechanical behavior of lithosphere at plate boundaries has been considered to be a challenging issue due to plate tectonics. Anatolia consists of several oceanic and continental fragments that were gathered into a single landmass in the last 400 million years. As a result of relative movements of surrounding plates, Turkish plate is taking its form continuously. This formation process yields several major shear zones such as the NAFZ, which is an active right lateral transform fault (Ketin, 1948; McKenzie, 1972). The NAFZ forms about 1600 km long boundary between Eurasia and Anatolia and has been the focus of intense geophysical and geological investigations. Throughout the history, the NAFZ has yielded sequences of several destructive earthquakes. As Barka (1996) stated, there is a westward migration of earthquake sequence on the NAFZ, which started with the 1939 Erzincan earthquake in eastern part. Last two of these disastereous earthquakes; 1999 Düzce (Mw=7.2) and 1999 Izmit (Mw=7.4) took place at the western part of the NAFZ.

1.2.1 Tectonic setting

Mainly, active tectonics of Anatolia is driven by the interactions of African, Arabian and Eurasian plates. The dominant factor is the convergent motion of African and Arabian Plate with respect to the Eurasian Plate after the Cenozoic closure of the Tethys Ocean (McKenzie, 1972; Dewey and Şengör, 1979; Taymaz et al., 1990). While Arabian Plate has a north-northwestern direction with a rate of about 18-25 mm/yr, African Plate has a north directed movement with a rate about 10 mm/yr (McClusky et al., 2000). This 10-15 mm/yr difference in movement rates gives rise to the escape of Anatolia towards west. Furthermore, the ‘pull’ due to the subduction of the African lithosphere along the Hellenic arc in the west and ‘push’ from the convergent zone in the east together act on Turkish plate to move southwestward along EAFZ and NAFZ (Taymaz et al., 2004; Taymaz et al., 2007).

The NAFZ extends from Karlıova Junction in the east to the Aegean in the west lying across the entire northern Turkey as it accommodates most of the westward movement of the Anatolian plate. Starting from its eastern end, the NAFZ runs along almost uncomplicated route for almost 1500 km and it splits into two branches in the western part. The northern strand crosses the Adapazarı Basin and passes through the Marmara sea reaching the Gulf of Saros while the southern branch comprises the Geyve Basin

and Lake Iznik (Barka & Kadinsky-Cade., 1988; Duman et al., 2005; Şengör et al., 2005). These branches have been slipping with rates of approximately 16 and 9 mm/yr respectively (e.g. Stein et al., 1997). Northern and Southern strands of the NAFZ forms natural boundaries among Istanbul-Zonguldak, Armutlu-Almacık, and Sakarya Zones. Istanbul-Zonguldak Zone represents the northernmost part of western Pontides. Armutlu-Almacık Zone is positioned in the Armutlu Peninsula and continues to the east to Almacık and Sünnice Mountains. Boundaries of this zone are delimited by active faults, nearly all of which have ruptured over the past century, during the 1944 Bolu-Gerede, 1957 Abant, 1967 Mudurnu Valley, 1999 İzmit, and 1999 Düzce earthquakes (Barka, 1992; Kondo et al., 2005, 2010; Duman et al., 2005; Pucci et al., 2007). During the Late Miocene, because of the volcanic activities and major faulting the landmass crumbled into smaller blocks and they were developed independently. For instance a pull-apart basin, Kuzuluk Basin with a very heterogeneous nature can be observed near the western edge of zone due to a west-east extensional deformation (e.g. Greber 1997). Lastly, Sakarya Zone is located in between Armutlu-Almacık Zone in the north and İzmir-Ankara Suture in the south. Active tectonics of Anatolia and its adjacents and the study area are shown in Figure 1.1a and Figure 1.1b, respectively.

1.2.1 Geological overview

Turkey is characterized by very complex geologic features which are mainly three tectonic units: the Pontides, the Anatolides-Taurides and the Arabian Platform (Ketin, 1966). The Pontides exhibit Laurasian characteristics and following the closure of Tethys Ocean they are separated by the İzmir-Ankara-Erzincan suture from the Anatolides-Taurides. The Pontides comprises the northern part of İzmir-Ankara-Erzincan suture and show evidence of Carboniferous and Triassic orogenities. Strandja, Istanbul and Sakarya are three terranes of the Pontides that have experienced various geological evolutions (Okay et al., 2008). Strandja Massif located in northwestern Turkey, has basement consists of mostly quartzo-feldspathic gneisses intruded by Late Carboniferous and Early Permian granitoids (Okay et al., 2001; Sunal et al., 2006).

The Istanbul-Zonguldak Zone is 400 km long and 55 km wide terrane that is a continental fragment located on the southwestern margin of the Black Sea which also belongs originally to the Scythian platform of Laurasia (Okay et al., 2008). It consists

of a late Precambrian crystalline basement which consists of gneiss, amphibolite, metavolcanic rocks, metaophiolite and granitoids (Chen et al., 2002; Yiğitbaş et al., 2004; Ustaomer & Robertson, 2010). In contrast to Istanbul-Zonguldak Zone, Sakarya Terrane exhibits sedimentary sequence starting from Lower Jurassic sandstones which rest on subduction-accretion complex of Triassic age basement (e.g. Şengör & Yılmaz, 1981; Okay & Tüysüz, 1999). The Armutlu-Almacık zone is located between two branches mostly involves pre-Jurassic basement of Sakarya Zone. This zone is made up of varying metamorphic rock associations that were amalgamated prior to the deposition of the Upper-Campanian-Maastrichtian successions (Şengör & Yılmaz, 1981). The Armutlu-Almacık Zone can be interpreted as the metamorphic equivalent of the northern part of Sakarya Zone which was metamorphosed during the collision of Sakarya and Istanbul-Zonguldak zones. Within the NAFZ in between Geyve Gorge to the west and Bolu area to the east, there are a few scattered outcrops of ophiolites with Late Cretaceous age which are considered as the remnants of Intra-Pontide suture zone (Şengör & Yılmaz, 1981). The Intra-Pontide suture is considered as the remnant of Paleotethyan Ocean floor that survived until the Late Cretaceous (Yılmaz & Tüysüz, 1997).

1.3 Early Studies

There have been numerous, intensive investigations involving the NAFZ due to the complexity of the plate interactions and associated continuous deforming nature of the crust along the zone. At the offshore segments of the NAFZ in the northern Sea of Marmara, micro-seismic activity is intensively monitored (e.g. Taymaz et al. 2001; Bulut et al. 2012; Bohnhoff et al. 2013). Observed travel times of seismic waves (e.g. P- and S-waves) extracted from the digital waveforms of ongoing seismic activity have been used to perform local tomography studies (e.g. Nakamura et al., 2002; Yolsal-Çevikbilen et al., 2012; Polat et al., 2016). More than 900 km of the NAFZ is dislocated in the twentieth century and to be able to investigate 3-D crustal heterogeneities due to this progressive rupture that causes long-term relative motion of crustal blocks along the faults, some studied active source tomography (e.g. Karabulut et al., 2006; Bayrakci et al., 2013) in the region. More recently crustal images resolved after both travel-time derived (e.g. Koulakov et al., 2010) and full waveform fitting-based regional tomography studies (e.g. Fichtner et al., 2013a,b; Çubuk-Sabuncu et al., 2017)

suggested the crust in the western NAFZ is characterized by low V_p and V_s , and high V_p/V_s ratios.

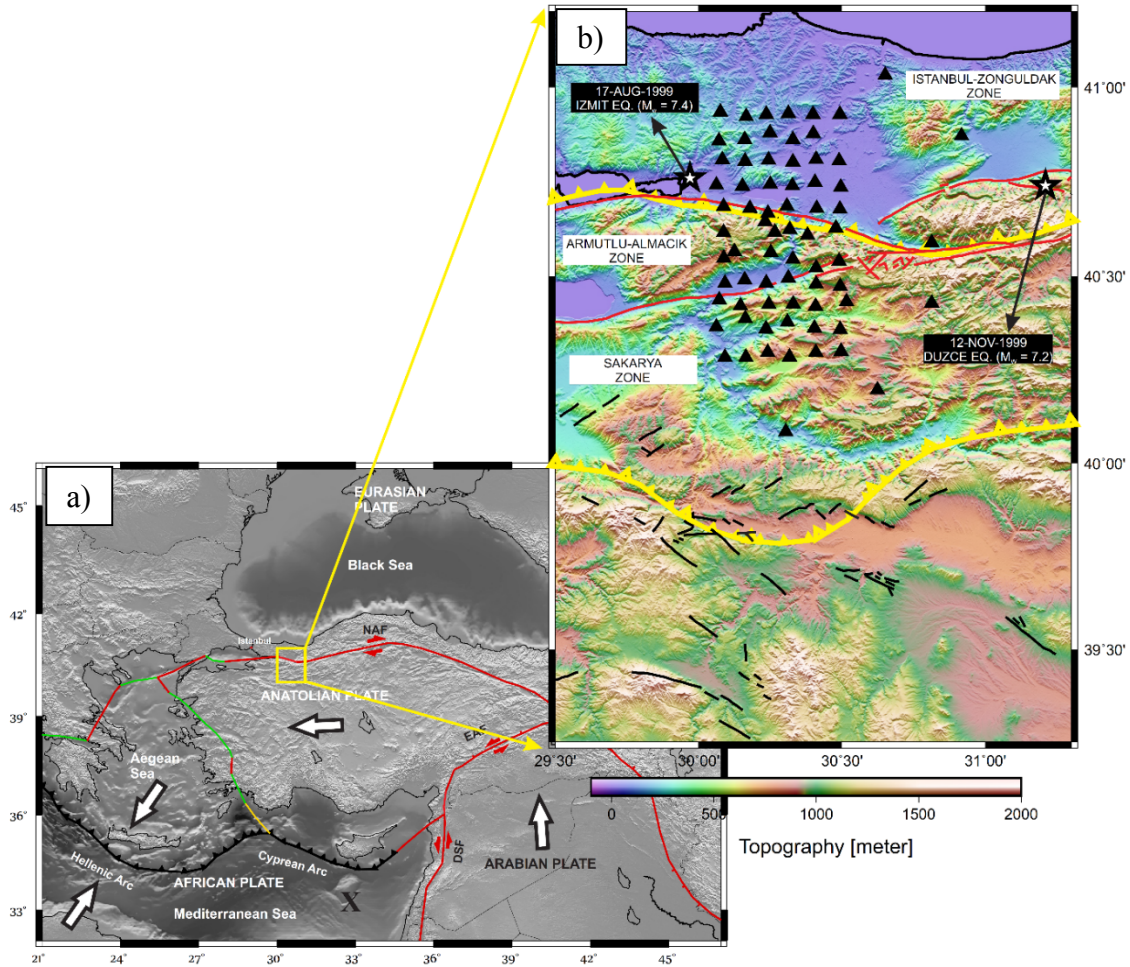


Figure 1.1. (a) Tectonic settings of Anatolia and surrounding regions. Major shear zones shown in red (NAF: North Anatolian Fault, EAF: East Anatolian Fault, DSF: Dead Sea Fault) Yellow rectangle represents study region (b) Tectonic boundaries shown in yellow, NAFZ in red and black framed white stars are İzmit and Düzce Earthquakes. KB: Kuzuluk Basin. Black triangles are 71 broadband stations of DANA network.

Within the framework of the DANA experiment (which is discussed in detail, on Section 2.), there are several geophysical investigations accomplished in the study area to reveal the crustal structure with different methodologies. For instance, Altuncu-Poyraz et al. (2015) observed a uniformly distributed microseismic activity within approximately 12 km depth range up to 20 km severally which is associated with the activity of major fault branches. Using ambient noise data analyses Warren et al. (2013) revealed that most crustal velocity variations are mostly correlated with the tectonic boundaries and suture zones. Thanks to small distances between stations in

DANA network, Papaleo et al. (2017) imaged the lithosphere using teleseismic tomography and revealed velocity variations within the lithosphere along the western part of the NAFZ. Kahraman et al. (2015) revealed a low velocity zone in between northern and southern branches of the NAFZ, with applying P receiver function (P-RF) analyses and ended up with very similar results to the lithological contrasts. They suggested that with the help of higher rates of penetration depths with P-RF studies, the depth extent of the deformation along the northern strand is much deeper. While the seismogenic zone that accommodates co-seismic displacements after 1999 Izmit earthquake, covers shallower depth range than approximately 20 km, a sub-vertical zone of shear localization, which possibly moves steadily at slow rates below the seismogenic zone in the upper crust down to Moho depths (Houseman, 2017).

Not only seismological studies but also geoelectrical properties have been investigated along the study region. Particularly, magnetotelluric imaging technique revealed asperities with varying resistivity along the western part of NAFZ (e.g. Elmas & Gürer, 2004; Tank et al., 2005; Kaya et al., 2009; Kaya et al., 2013). For instance, Tank et al. (2005) revealed that, a conductive body exists at 30 to 50 km depth between two branches of NAFZ due to the presence of partial melting while Kaya et al. (2013) identified that in between two strands there are larger resistivity values indicating the saturation of fractured rocks. Moreover, at upper crustal depths, the Istanbul-Zonguldak Zone to the north and Sakarya Zone to the south identified by relatively resistive structures (Kaya et al., 2013; Tank et al., 2005).

There are several studies trying to identify the crustal structure in different regions all around the world with same methodology of this study by means of seismic attenuation properties. For instance, Eulenfeld & Wegler (2016) developed an improved method to separate intrinsic and scattering attenuation to investigate the area near three geothermal reservoirs in Germany from 1 to 70 Hz frequencies. They revealed a comparison of scattering and intrinsic attenuation between sedimentary sites and crystalline rocks. Furthermore, Eulenfeld & Wegler (2017) investigated the areal distribution of crustal intrinsic and scattering attenuation of shear waves along United States with 25000 events. They observed a west-east decline of intrinsic attenuation for high frequencies and interpreted this as the transition from young, hot to old and cold crust while scattering attenuation is stronger in the east. However, their results of low frequencies did not show trends. Also, Gaebler et al. (2015a) studied the crustal structure beneath western Bohemia/Vogtland in Czechia with fitting the synthetic and

observed seismograms and determined the scattering and absorption parameters. The seismic attenuation based on coda wave analyses was investigated at local and regional scale along the NAFZ in Anatolia and Middle East (e.g. Pasyanos et al., 2016; Sertcelik & Guleroglu, 2017; Gaebler et al., 2018). Sertcelik & Guleroglu (2017) observed the largest change of Q_c with lapse time along the NAFZ from east to west at the western edge in the Yalova-Saros region as this implies the significance of regional heterogeneity. To be able to further constrain, in particular, the upper crust we map 2-D variations of frequency-dependent seismic attenuation properties in the region. In this respect, new findings will be complementary with inconclusive seismic studies along the NAFZ as it contributes to future crustal models that can reasonably high/low intrinsic and scattering attenuation in the region.

1.4 . Seismic Coda Waves

In the early 1970s, a pioneer of modern seismology Keiiti Aki introduced the coda waves to the scientific community. Coda waves are considered as the energy loss of a seismic wave due to randomly distributed heterogeneities within the Earth and corresponds to the later portions of seismograms after the direct arrivals such as P- and S-waves (Figure 1.2). For the analysis of seismic waves, laterally homogeneous media assumption is considered adequate for the long period waves. However, short period seismic waves suffer strongly from lateral heterogeneities. Unlike direct waves, coda waves were found to be more advantageous in earthquake source characterization compared to the direct waves since they samples the entire region averaging a volume around the focal sphere as this makes these waves almost insensitive to any source radiation pattern effect (e.g., Aki, 1969; Aki & Chouet, 1975; Mayeda et al., 2003). In this section firstly the concept of scattering energy in the seismic coda and general principles of the Radiative Transfer Theory that is used to represent scattered coda wave energy will be presented. Later, we will mention about the advantages of coda waves and historical background approaches in seismology using these wave types.

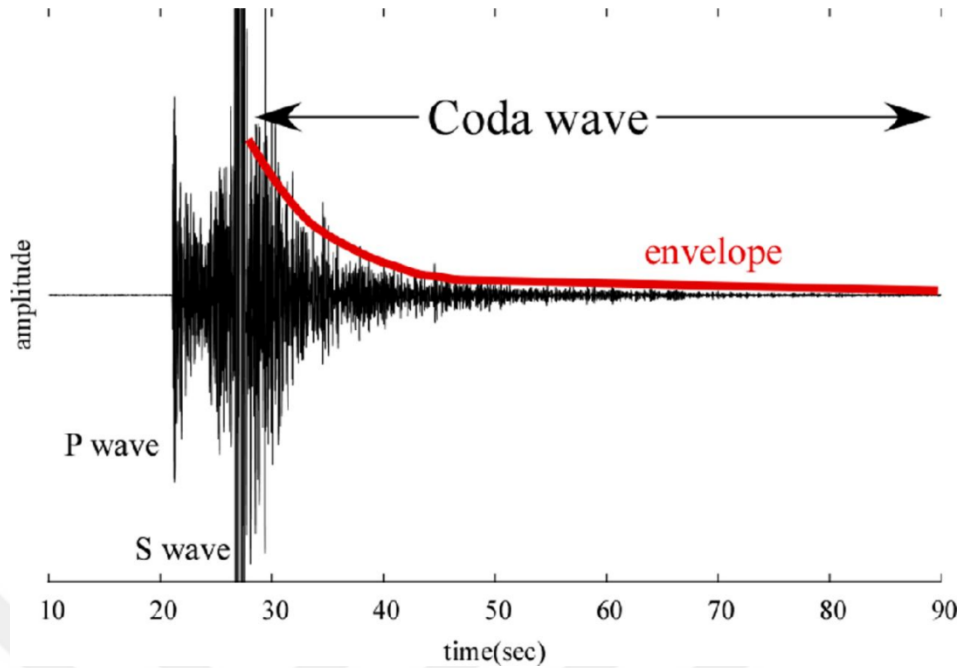


Figure 1.2. A waveform example shows direct P- and S-waves, coda portion of the seismogram and the coda envelope (Okamoto et al., 2013).

1.4.1 Scattering energy

The decaying energy with time of coda waves varies with the geological properties of the crustal structure and the investigated frequency band. The energy density corresponds to the amount of energy that passes through a unit area per unit time as shown in Figure 1.3 (Sato et al., 2012).

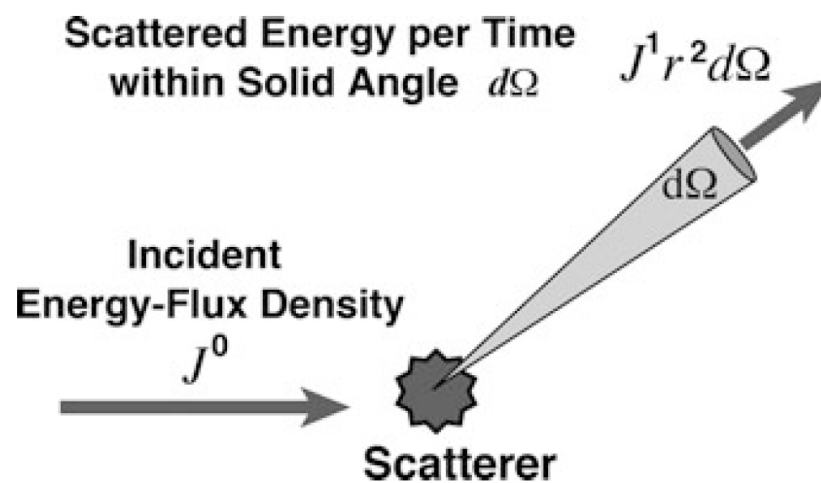


Figure 1.3. Illustration of scattering energy representation from a scatterer (Sato et al., 2012).

In Figure 1.3, J^0 is the energy-flux density that encounters a scatterer forming spherical outgoing waves with energy J^1 . $d\Omega$ represents the given solid angle element where the amount of energy scattered per unit time is $J^1 r^2 d\Omega$ where the term $r^2 d\Omega$ corresponds to the surface element. Then, the differential scattering over the scatterer can be given as the following ratio;

$$\frac{d\sigma}{d\Omega} = \frac{J^1 r^2}{J^0} \quad (1.1)$$

However, in real crustal structure, the scatterers are randomly distributed and in order to model such structure the media is considered as being randomly homogeneous with n number of point like scatterers. Then the scattering g can be given as in equation 1.2.

$$g \equiv 4\pi n \frac{d\sigma}{d\Omega} \quad (1.2)$$

Scattering g , given in equation 1.2, varies with the frequency and it depends on the scattering angle. However, for a more realistic approach the total scattering coefficient should be defined by the average at all directions.

1.4.2 Coda excitation models

There are several models to explain the energy density, time dependence and attenuation information hidden coda waves. Firstly, Aki & Chouet (1975) proposed two models: back scattering and diffusion models. Then, Frankel & Wennenberg (1987) proposed energy flux model. In this study we employ acoustic RTT.

1.4.2.1 Single back-scattering model

In order to explain the time dependence of scattered energy in 3D medium Aki & Chouet (1975) proposed single back-scattering model (Figure 1.4) in which the receiver and the source are assumed to be in the same spot and r is the distance between them and the scatterer. The incident energy flux density coinciding with a scatterer from a total energy W is given as follows (Sato et al., 2012);

$$\frac{W}{4\pi r^2} \delta\left(t - \frac{r}{v_0}\right) \quad (1.3)$$

where delta function, δ represents the time delay. Backscattering is shown by:

$$\frac{W}{4\pi r^2} \delta\left(t - \frac{2r}{v_0}\right) \frac{1}{r^2} \frac{d\sigma}{d\Omega} \quad (1.4)$$

Because of the random scatterers are incoherent, the summation is needed from individual scatterers in equation 1.4, and the energy flux-density divided by velocity V_0 will provide energy density as given in equation 1.5:

$$E(x = 0, t) = \sum \frac{W}{4\pi r^2} \delta\left(t - \frac{2r}{v_0}\right) \frac{1}{r^2} \frac{d\sigma}{d\Omega} \frac{1}{v_0} \quad (1.5)$$

Then with the substitution of $g_\pi = 4\pi n \frac{d\sigma}{d\Omega}$ and addition of the attenuation with an angular frequency ω , the equation 1.6 is provided.

$$E(x = 0, t) = \frac{W g_\pi H(t)}{2\pi v_0^2 t^2} e^{-Q_c^{-1} \omega t} \quad (1.6)$$

where $H(t)$ and Q_c^{-1} indicates Heaviside step function and coda attenuation factor, respectively.

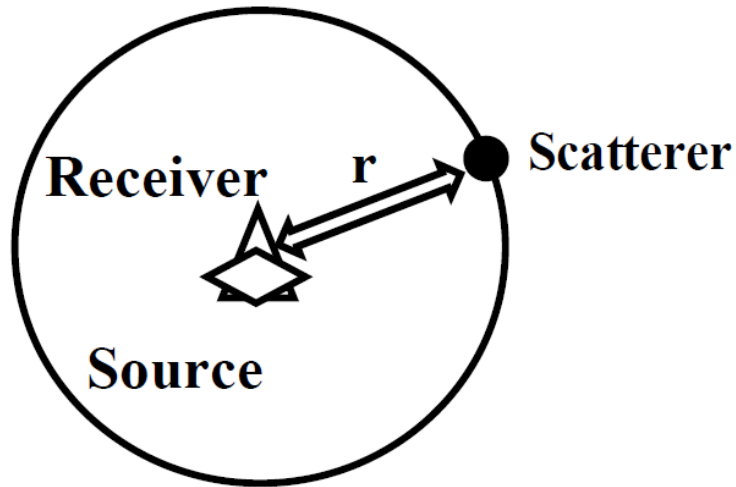


Figure 1.4 Simple illustration of single back-scattering model for a common source and receiver location. Distance between the source and scatterer represented as r .

1.4.2.2 Diffusion model

At large lapse times multiple scattering becomes dominant due to the fact that direct energy becomes smaller and energy density is seen to have smooth spatial distribution. Morse & Feshbach (1953) proposed the diffusion equation by:

$$(\partial_t - D\Delta)E(x, t) = W\delta(x)\delta(t) \quad (1.6)$$

Here, diffusivity $D = V_0/3g_0$ and the analytical solution to the equation 1.6 is given as follows:

$$E(x, t) = \frac{WH(t)}{(4\pi Dt)^{3/2}} e^{-\frac{r^2}{4Dt}} \quad (1.7)$$

By adding the attenuation parameters into equation 1.7, diffusion model solution will be obtained as:

$$E(x, t) = \frac{WH(t)}{(4\pi Dt)^{3/2}} e^{-\frac{r^2}{4Dt}} e^{-Q_c^{-1}\omega t} \quad (1.8)$$

Diffusion approximation is beneficial in acoustic RTT to represent multiple scattering regimes as well as anisotropic regimes.

1.4.2.3 Energy-flux model

Frankel & Wennerberg (1987) used a 2D finite difference scheme to simulate the scattered energy that is spreading behind the direct wave. Their model results were very consistent with observations on seismograms. They proposed this model for spatiotemporal distribution of energy density. It cannot explain the energy spread of scattered waves in space but provides an approach considering multiple scattering and causality. Model is illustrated in Figure 1.5.

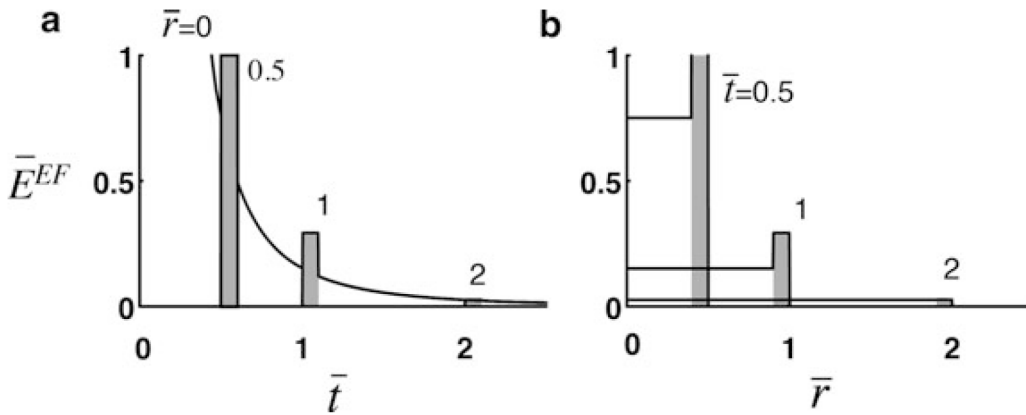


Figure 1.5. Illustration of energy flux model. (a) time traces at different scaled distances (b) spatial distribution of normalized energy. The shaded area represents the direct wave energy density (Sato et al., 2012).

With a simple combination of intrinsic and scattering attenuation, energy-flux model can be defined by equation 1.9:

$$E(x, t) = \frac{3W(1-e^{-Qs^{-1}\omega t})e^{-Qi^{-1}\omega t}}{4\pi(V_0 t)^3} H\left(t - \frac{r}{V_0}\right) \quad (1.9)$$

where the $e^{-Qs^{-1}\omega t}$ term represents the direct energy decay at angular frequency ω , due to scattering attenuation with increasing lapse time whereas $e^{-Qi^{-1}\omega t}$ is the intrinsic absorption. The H is the Heaviside step function and $\mathbf{r} = |\mathbf{x}|$.

1.4.2.4 Radiative transfer theory

RTT is one of the most common methods to illustrate the seismic wave propagation in a scattering medium (e.g. Figure 1.6). It was firstly introduced by Chandrasekhar (1960) to the scientific community in order to describe the propagation of light through a turbulent atmosphere and later adapted into field of seismology. In this thesis, we modelled the energy densities by applying acoustic RTT due to several reasons. Earlier Gaebler et al. (2015b) compared crustal scattering and intrinsic attenuation parameters obtained using anisotropic elastic and isotropic acoustic approaches by calculating the transport mean free path (l_s^*) coefficients. Transport mean free path coefficients considered as the combination of misfit and correlation length. They highlighted that these two scattering parameters can not be obtained separately by elastic simulations. In conclusion, their results with both methods yielded similarly and acoustic approach found to be more practical in terms of having analytical solutions. Eulenfeld & Wegler (2016) assured that choosing acoustic isotropic case when calculating Green's functions could provide computationally much cheaper solution. Furthermore, the analytic approach of the solution for isotropic radiative transfer can be used for simplicity (e.g. Paasschens, 1997; Eulenfeld & Wegler, 2016).

Specific intensity $I(\mathbf{n}, \mathbf{r}, t)$, which is the central quantity in the RTT, describes the angularly resolved energy flux from a radiating surface located at a position \mathbf{r} into an unit solid angle around direction \mathbf{n} at time t and this transportation problem can be considered as the conservation of energy.

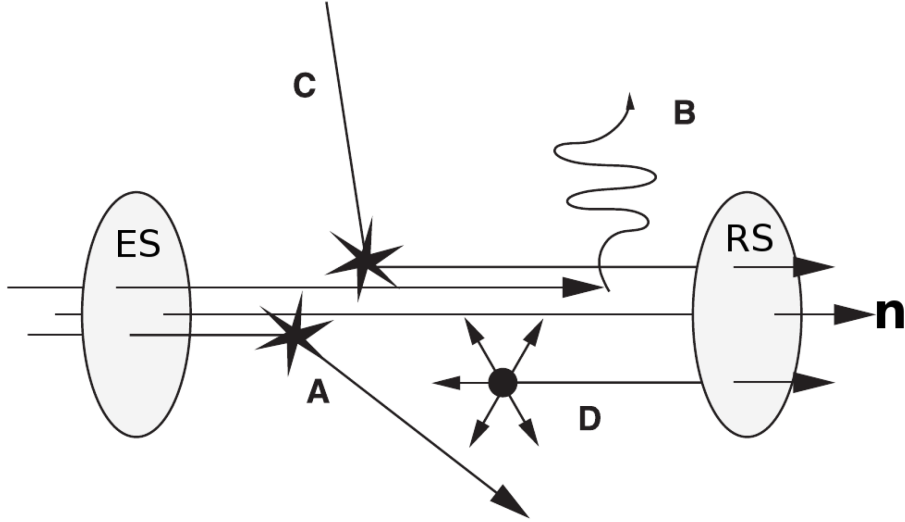


Figure 1.6. Energy flux in RTT. Energy is emitted from the emitting surface (ES) through the receiving surface (RS) around a direction of \mathbf{n} . In addition to this pattern, some portions of the energy are reduced by scattering through other directions (A), dissipation (B) but flux can increase by scattering from other directions gathers into the direction \mathbf{n} (C) and scatterers from another sources along the path (D) (Gaebler, 2015).

When the transfer is considered as acoustic, the change of intensity along an infinitesimal path element δs is given as follows:

$$\frac{\delta}{\delta s} I(\mathbf{n}, \mathbf{r}, t) = -(g_0 + b)I(\mathbf{n}, \mathbf{r}, t) + \int_{4\pi} g(\mathbf{n}', \mathbf{n}) I(\mathbf{n}', \mathbf{r}, t) d\Omega_{n'}, \quad (1.10)$$

where the incident direction is the unit vector \mathbf{n} and all other directions are introduced as \mathbf{n}' . g_0 is the parameter for scattering energy away from direction \mathbf{n} , while $g(\mathbf{n}', \mathbf{n})$ is the scattering of energy from all directions into direction \mathbf{n} . The absorption of energy is described by the parameter b . Equation 1.10 implies that a reduction of intensity can be achieved by the contribution of both intrinsic attenuation and scattering of energy. In addition, the specific intensity is restated to the energy density with velocity given as follows:

$$a(\mathbf{n}, \mathbf{x}) = \frac{1}{v} I(\mathbf{n}, \mathbf{r}) \quad (1.11)$$

where $a(\mathbf{n}, \mathbf{x})$ is the angularly resolved energy density and v is the velocity of the ray. Because the energy transport in seismology is always a non-stationary problem and the media is static, specific intensity can also depends on frequency rather than time meaning that the frequency along the ray is conserved (Sens-Schönfelder et al., 2009).

Energy propagation is modeled in a half space medium with an isotropic shear wave source and to do so, first the transfer of energy is considered in full space of which

details is given in Sato et al. (2012) and explained with the energy density Green's functions given in equation 1.12.

$$G(\mathbf{r}, t) = F(\mathbf{r}, t) + v_0 g_0 \int_{-\infty}^{\infty} dt' \iiint d\mathbf{r}' F(\mathbf{r} - \mathbf{r}', t - t') G(\mathbf{r}', t') \quad (1.12)$$

where v_0 denotes average velocity of S-waves and g_0 denotes total scattering coefficient. $r = |\mathbf{r}|$ represents the distance between the source and receiver. Green's function of the coherent wave energy $F(\mathbf{r}, t)$ is defined in equation 1.13.

$$F(\mathbf{r}, t) = \frac{1}{4\pi v_0 r^2} H(t) \delta\left(t - \frac{r}{v_0}\right) e^{-v_0 g_0 t} \quad (1.13)$$

Here, H stands for Heaviside step function. By interpolating the explicit solutions of radiative transfer in 2D and 4D. The solution derived by Paasschens (1997) then reads as in equation 1.14.

$$G(r, t, g_0) = e^{-v_0 g_0 t} \left[\frac{\delta(r - v_0 t)}{4\pi r^2} + \left(\frac{4\pi v_0}{3g_0}\right)^{-\frac{3}{2}} t^{-\frac{3}{2}} \right. \\ \left. * \left(1 - \frac{r^2}{v_0^2 t^2}\right)^{\frac{1}{8}} K\left(v_0 g_0 t \left(\left(1 - \frac{r^2}{v_0^2 t^2}\right)^{\frac{3}{4}}\right)\right) H(v_0 t - r) \right]$$

$$\text{where the function } K(x) \cong e^x \sqrt{1 + \frac{2.026}{x}} \quad (1.14)$$

The term with Dirac delta δ , in equation 1.14 stands for the direct wave, the other parts are related to scattered waves. However, for real media, isotropic scattering is not realistic, so the scattering coefficient g_0 should be determined as g^* as transport scattering coefficient for the assumption of more realistic anisotropic scattering (Gaebler et al., 2015a).

Then modeled energy density can be obtained from the multiplication of Green's functions $G(r, t, g^*)$, spectral source energy W , energy of site amplification factor $R(r)$, and exponential expression of intrinsic attenuation parameter, b as given by:

$$E_{mod}(t, r) = WR(r)G(r, t, g^*)e^{-bt} \quad (1.15)$$

Dimensions for E_{mod}, W, R, G are, $Jm^{-3}Hz^{-1}, JHz^{-1}, 1, m^{-3}$ respectively. In equation 1.15, b and g^* are directly related to the quality factors of intrinsic Q_i^{-1} and

scattering Q_s^{-1} attenuation, respectively (Gaebler et al., 2015a). In equation 1.16, quality factors are defined as follows:

$$Q_s^{-1} = \frac{g^* v_0}{2\pi f} \quad Q_i^{-1} = \frac{b}{2\pi f} \quad (1.16)$$

where f represents the frequency while v_0 represents the mean shear wave velocity. Each transport scattering coefficient and absorption parameter are converted to quality factors of intrinsic Q_i^{-1} and scattering Q_s^{-1} attenuation factors and calculated independently.

1.4.3 Historical background on coda wave approaches

Aki (1969) showed that amplitude of the coda waves and their spectral content might provide source excitation characteristics of a given earthquake. Aki & Chouet (1975) suggested that the spectral content of the coda of a local earthquake is nearly identical for all stations unlike the body waves and decay of coda power spectra is not sensitive to the source-receiver distance or raypath. They also introduced the coda parameter Q_c , which defines the decrease in amplitude of coda waves and argued that Q_c depends on attenuation due to anelastic energy loss. Aki & Chouet (1975) also interpreted coda waves as back-scattered waves from heterogeneities randomly distributed within the lithosphere and proposed two models to explain generation of coda waves. First model is single backscattering and the second is diffusion model, which were already discussed in section 1.4.2. Following the work of Aki & Chouet (1975) on coda waves using local events, Nakamura (1977) and Dainty & Toksöz (1981) studied coda waves of lunar seismograms and their results were suggesting that diffusion model of Aki & Chouet (1975) could be only valid for moon's crust due to strong scattering. In addition to these there are some Q_c studies that have observed temporal and spatial change of coda values as they provided valuable information of forthcoming earthquakes (e.g. Gusev & Lemzikov, 1985; Sato et al., 1988; Jin & Aki, 1989).

There are several approaches based on coda wave analyses in order to study the source properties and site effects. One empirical and robust approach is Coda Normalization Method (CNM) and depends on the assumption that the coda energy does not change in some portion of surrounding media over the source. For instance, Tsujiura (1978) and Tucker & King (1984) used the CNM to estimate the site amplifications of coda

and S waves as a function of frequency for the same source and revealed that site amplifications for both wave types are same in between 0.75 and 24 Hz frequencies. Hoshiya et al. (1993) used another approach, Multiple Lapse Time Window Analysis (MLTWA), to investigate frequency dependent site amplifications by assuming that the decay of coda does not depend on the distance between the source and receiver but the scattering. They suggested that the local geology of the region that includes the station is the only variable that affects coda. In the same year, Mayeda et al. (1991) studied coda waves and calculated site amplifications in six frequency bands with respect to a reference site. They proposed that at higher frequencies site amplification could be unstable due to the geological difference in near surface. Later, Koyanagi et al. (1992) used S-coda waves as a tool to investigate site properties in relation to the subsurface lava flow characteristics in Hawaii using a frequency range varying between 1.5 to 15 Hz. Hoshiya (1997) studied the seismic coda envelope to elucidate depth-dependent velocity structure of S waves and suggested that energy density of coda waves varies due to velocity discontinuities. Furthermore, he discussed that the CNM may not be successful for the crustal structures that have a strong depth-dependence of velocities, absorption and scattering.

Bianco et al. (2002) examined the coda-Q properties in the Southern Apennine zone to investigate intrinsic and scattering attenuation by applying the MLTWA and showed that general trend of Q_c^{-1} is similar to that of Q_i^{-1} and values for Q_s^{-1} are relatively smaller for the frequency range between 2 to 12 Hz. They concluded that intrinsic attenuation is dominant over scattering in the study area. Vargas et al. (2004) investigated the spatial variation of coda waves in northwestern Colombia by performing single scattering method. They estimated intrinsic and scattering attenuation parameters separately via the used MLTWA. Their results have shown some discrepancies between synthetic and observed models but mostly intrinsic attenuation was found to be dominant on the area.

Mayeda et al. (2003) proposed an empirical method that considered a transfer function from S- to coda waves. They applied a band-pass filtering in 14 narrow frequencies ranging from 0.02 to 8 Hz on the waveform data extracted from local and regional earthquakes. In this method their aim was to estimate seismic moment of those earthquakes using moment-rate spectra that could be calibrated using some reference events whose seismic moment values are already known to scale the dimensionless coda amplitudes.

Sens-Schönfelder & Wegler (2006) proposed a new technique to obtain source spectra and seismic moments for regional earthquakes. For a given source-receiver pair, they did not use coda normalization but instead used analytical equation of coda waves based on the RTT to invert for simultaneously source properties, site response factors as well as separated intrinsic and scattering attenuation parameters. Using the same methodology, Gaebler et al. (2015a) compared the results obtained from acoustic and elastic radiative transfer theory in W-Bohemia/Vogtland region. They studied 14 shallow events and revealed that both acoustic and elastic simulations would yield similar results for crustal parameters. Later on, Eulenfeld & Wegler (2016,2017) utilized isotropic acoustic RTT to separate intrinsic and scattering attenuation. Their results showed that their non-empirical envelope inversion technique was successfully working on crustal structure by even providing additional source properties such as moment magnitudes of each analysed earthquake.

2. DATA

Here we will present the details of the data utilized in this study. In this thesis, we focused on the western part of NAFZ benefiting from broadband seismic waveforms from a dense temporary network, which was mainly deployed to image the crustal structure properly within the framework of FaultLab project. The Dense Array for Northern Anatolia (DANA) was operated from May 2012 to September 2013 with collaboration of University of Leeds, Kandilli Observatory, Sakarya University and UK Natural Environment Research Council. 71 broadband stations with 7 km nominal spacing recorded data continuously at 50 sps. The waveform data were extracted based on an earthquake catalogue published in Altuncu-Poyraz et al. (2015). At first we examined the waveforms by visual interpretation and pick the local earthquakes and those not effected by noise. Also we eliminated the regional events recorded in Seismic Analysis Code (SAC) (Goldstein et al., 1998). An example of this picking process is shown in Figure 2.1.

In total, we examined 1315 events with local magnitudes (M_l) varying from 0.1 to 4.1. In order to avoid the undesired effects of Moho boundary guided Sn-waves we took station-event pair distance as less than 120 km. The effects from lower crust and upper mantle are reduced by selecting events with less than 10 km focal depths. In the end of this selection criteria, our event number became 1035. Station-event pairs, their locations and the raypaths are given in Figure 2.2a.

Following the decision on possible earthquake-station pairs, we created xml and quakeml files which are necessary for the python based framework ObsPy (e.g. Beyreuther et al., 2010) prior to further processing of seismological data. The data were filtered in five frequency bands and to achieve this used a Butterworth band-pass filter with central frequencies at 0.75, 1.5, 3.0, 6.0 and 12.0 Hz and each inverted independently. Hilbert transform was used to determine the total energy envelopes from observed seismograms (see section 3.3 for more details). We used a crustal velocity model data which was earlier developed by Delph et al. (2015) to determine the P and S wave onsets on envelopes. Waveform data within the coda window part is

smoothed via 1s-Bartlett window to avoid potential influence of anisotropic scattering over the direct S-wave arrival that is not well defined in acoustic Green's function. To achieve including all direct S-wave energy, we set up the S-wave window as starting 3 s before the S-wave arrival and ends 7 s afterwards. The maximum length of coda window is chosen to be 100 s as it starts at the end of S-wave window. We excluded stations with coda windows shorter than 10 s.

To ensure the quality of analyzed waveforms, we applied a signal-to-noise ratio (SNR) threshold, for instance, length of coda window can be shorter if the SNR is below than a level of 2.5 or if the smoothed coda envelope does not decline with time but starts rising again (e.g. due to subsequent arrival of an aftershock). Finally, we obtained a total of 249 earthquakes satisfying the aforementioned data selection constraints prior to the inversion step (Figure 2.2b).

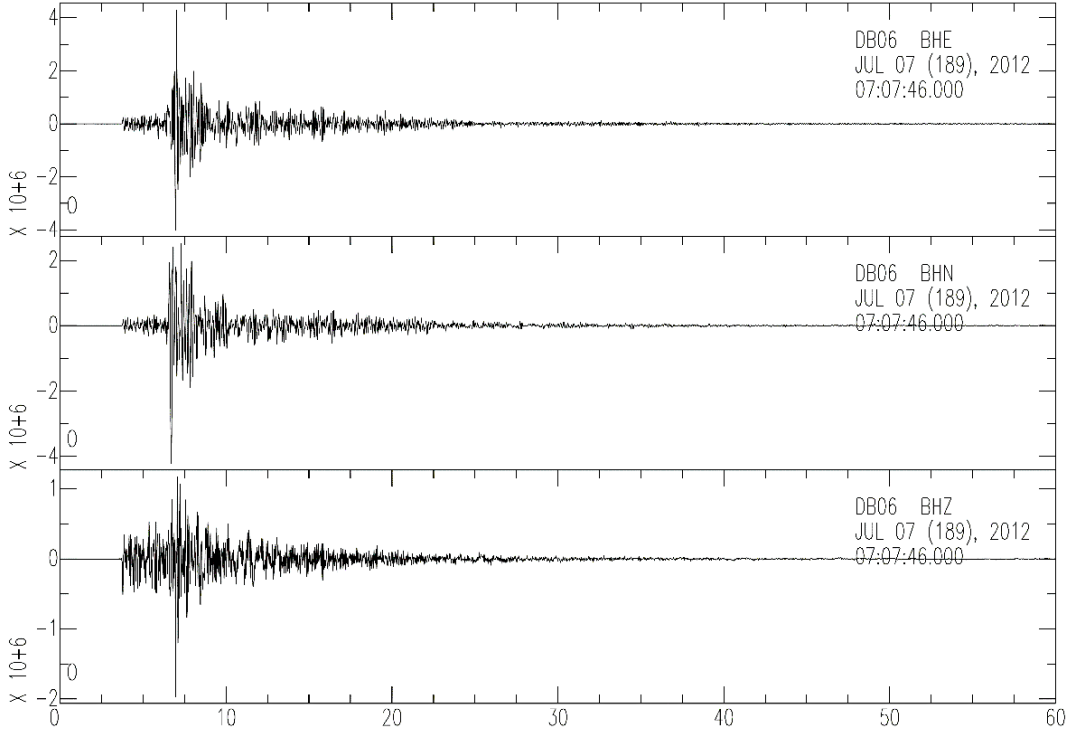


Figure 2.1. Visually selected 3-component waveform example in our dataset.

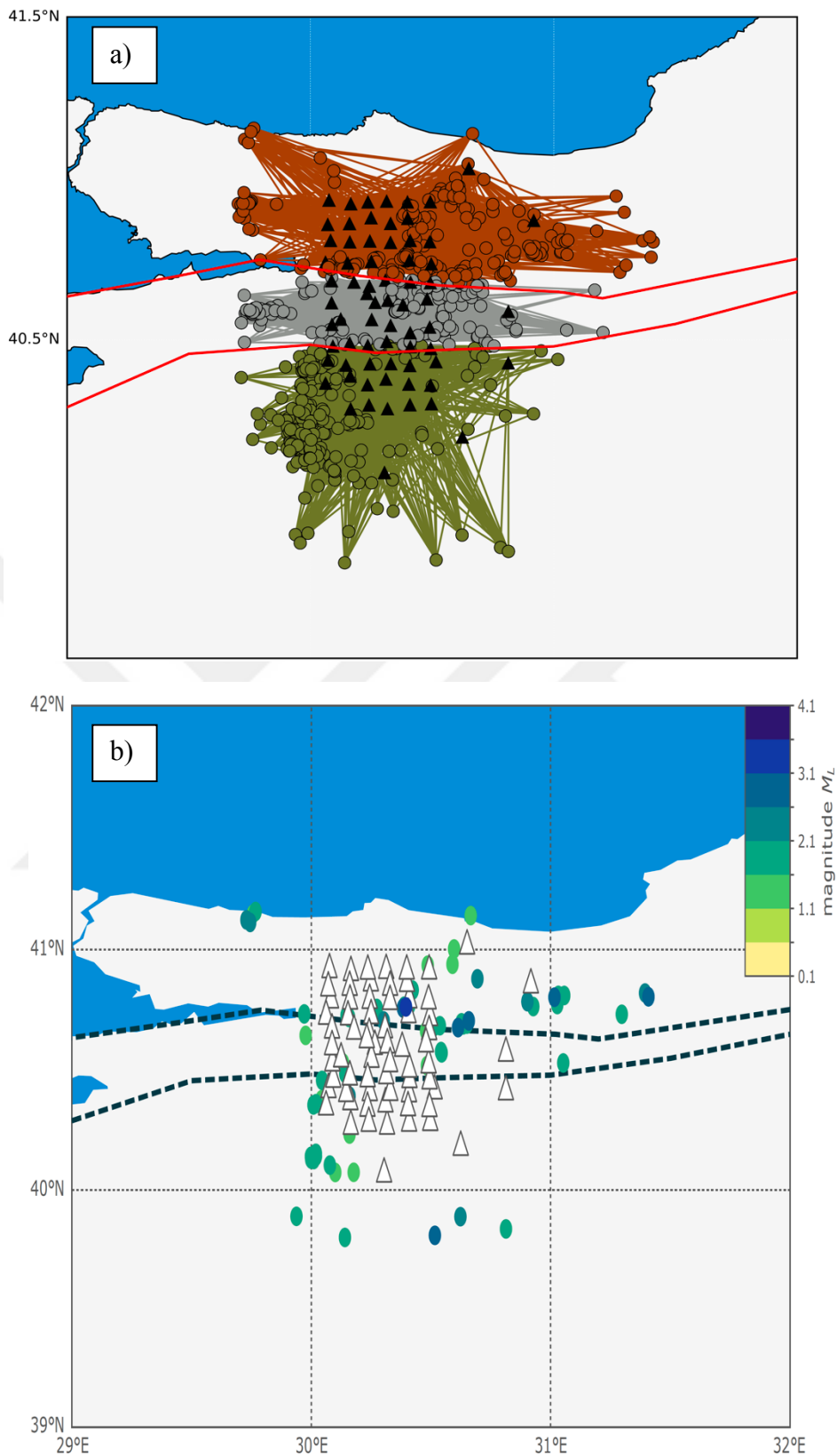


Figure 2.2. (a) 1035 earthquakes (circles) with three different colored ray paths according to their position relative to the NAFZ strands (red). 71 stations are given as black triangles. (b) 249 earthquakes (circles) coloured by their magnitudes. 71 stations are given as white triangles.



3. METHODOLOGY

3.1. General Remarks

Seismic waves carry valuable information along the raypath when propagating from source to receiver. Due to the fact that Earth is not perfectly elastic and homogeneous, seismic waves lose energy and attenuate with time. Thus, examining seismic wave attenuation at a given region is essential to investigate the physical characteristics of the inhomogeneities in the crust especially for high-frequency wave analyses. In addition to this, the amplitude of seismic waves decays exponentially with distance. The attenuation of seismic waves can depend on characteristics of the path and site effects in relation to the shallow and crustal structure as well as the size and source properties of the event (Trégourès et al., 2002).

Analyzing the high-frequency seismograms is extremely difficult because of the lateral heterogeneities. Several studies within the last few decades have proven that the using seismic coda waves could provide more robust frequency dependent attenuation properties as being decomposed into its intrinsic and scattering components compared to the direct waves due to its volume averaging sampling properties around the seismic foci (e.g. Aki, 1969; Aki and Chouet, 1975; Abubakirov & Gusev, 1990; Mayeda and Walter, 1996; Korn, 1997; Eken et al., 2004; Calvet & Margerin, 2013; Gök et al., 2016; Pasyanos et al., 2016). Yoo et al. (2011) have discussed that coda wave amplitude derivation following the coda normalization method is four to five times robust than those amplitudes derived from direct phases.

In this section, firstly seismic wave attenuation issue will be discussed. Then the details of inversion approach using the RTT for the forward calculations will be presented.

3.2. Separation of Intrinsic and Scattering Attenuation

Attenuation of the coda waves Q_c is the summation of anelastic energy loss Q_i and attenuation resulted from scattering Q_s . In other words, apart from geometrical

spreading, attenuation is a result of a combined process of absorption and redistribution of the energy. Intrinsic attenuation is the conversion of the seismic energy into other types of energy such as heat or mineral dislocations. The scattering attenuation is caused by the redistribution of the seismic energy due to existing small-scale heterogeneities.

3.3. Calculation of Observed Densities

In order to estimate the energy densities, which will form the observed data in coda wave studies, coda waves envelopes are established in different frequency bands applying Hilbert Transform \mathcal{H} on each band-pass filtered seismogram (\dot{u}_c). Then using equation 3.1, the mean square velocity $\langle \dot{u}^2 \rangle$ is estimated (e.g. Sato et al. 2012):

$$\langle \dot{u}(t, r)^2 \rangle = \frac{1}{2} \sum_{c=1}^3 (\dot{u}_c(t, r)^2 + \mathcal{H}(\dot{u}_c(t, r))^2) \quad (3.1)$$

Observed energy density is computed using the mean square velocity, the mean mass density (ρ_0) and filter width, Δf as follows:

$$E_{obs}(t, r) = \frac{\rho_0 \langle \dot{u}(t, r)^2 \rangle}{c \Delta f} \quad (3.2)$$

Here, C is taken as 1 for full space while it is taken as 4 to consider free surface correction, in practice, since the stations are located at the surface (Emoto et al., 2010).

4. INVERSION

4.1. Estimation of Attenuation Parameters

An optimum fitting between observed coda wave envelope at the station and modeled energy densities represented by synthetic envelopes that can be calculated using acoustic RTT is the main motivation of the inversion procedure. This allows scattering attenuation parameters and us to find source-receiver specific attenuation properties namely intrinsic. Here we notice that the role of intrinsic and scattering attenuation on the shape of coda wave envelopes is different. The effect of scattering can be measured via the energy ratio of the coda and the direct arrival while intrinsic attenuation has a control on the exponential decrease in the envelope. At this stage we follow the same inversion procedure introduced by Eulenfeld & Wegler (2016) that is restricted to isotropic sources with the source function composed of spectral source energy W and Dirac delta function ($W\delta(\mathbf{r})\delta(t)$). The energy density for a given frequency band can be computed as follows:

$$E_{mod}(\mathbf{t}, \mathbf{r}) = WR(\mathbf{r})G(\mathbf{r}, \mathbf{t}, \mathbf{g})e^{-bt} \quad (4.1)$$

In equation 4.1, $R(\mathbf{r})$ represents the site amplification factor, e^{-bt} is the exponential decrease caused by intrinsic attenuation. The vector \mathbf{g} stands for scattering parameter. $G(\mathbf{r}, \mathbf{t}, \mathbf{g})$ is the Green's functions for the direct and scattered waves. The optimization problem here depends on an algorithm that simultaneously inverts for a scattering and intrinsic attenuation parameters (e.g. \mathbf{g} and b) and spectral source energy W and site term R , which can give the best representation of observed coda wave envelope. Because of the multicollinearity between the site amplification and spectral source energy, we multiply the W_j by an arbitrary factor and divide R_i by it..

$$R_i = \frac{\widetilde{R}_i}{w_1} \quad W_j = \widetilde{W}_j w_1 \quad (4.2)$$

In equation 4.2, $\widetilde{W}_j=1$ by definition. However, to calculate W_1 another constrain is needed so we fixed the geometric mean (GM) of the site corrections to 1 and then, W_1 is calculated as in equation 4.3.

$$W_1 = \frac{GM(\widetilde{R}_i)}{GM(R_i)} = GM(\widetilde{R}_i) \quad (4.3)$$

We have already mentioned the calculation of observed energy envelopes in details in section 3.3.

Following the calculation of modeled envelope and observed envelopes for different frequency bands, inversion takes three steps listed below:

(i) A fixed scattering parameter \mathbf{g} is employed to compute Green's function described in equation 1.14. Then it involves a least square direct inversion scheme to solve for three unknown model parameters, b , R_i and W_j :

$$\ln E_{obsijk} = \ln G(t_{ijk}, r_{ij}, \mathbf{g}) + \ln R_i + \ln W_j - bt_{ijk} \quad (4.4)$$

(ii) Sum of the squared residual is calculated by inserting estimated b , R_i and W_j and selected \mathbf{g} into equation 4.5:

$$\epsilon(\mathbf{g}) = \sum_{i,j,k}^{N_S, N_E, N_{ij}} (\ln E_{obsijk} - \ln E_{modijk}(\mathbf{g}))^2 \quad (4.5)$$

Where, N_S corresponds to stations with index i , N_E is events with index j and N_{ij} corresponds to the observed energy densities for every event at each station with an index k for a certain frequency band.

These two steps (i) and (ii) are repeated for different fixed scattering parameters to obtain optimal parameters of W_j , R_i , b and \mathbf{g} by minimizing the misfit function (e.g. equation 4.5). This optimization process is illustrated in Figure 4.1.

We have performed a visual investigation on L2-norm coda envelope fits available frequencies at recording stations for each analyzed earthquake. This was necessary process to ensure whether we only include inversion results represented by the optimal fit. Figure 4.2 presents example fits for a specific earthquake at five different frequency bands (0.75, 1.5, 3.0, 6.0, 12.0 Hz) recorded at four stations Coda envelope fitting performance for the NAFZ were quite comparable with those earlier experienced in

other studies (e.g. Sens-Schönfelder & Wegler, 2006; Gaebler et al., 2015a; Eulenfeld & Wegler, 2016, 2017).

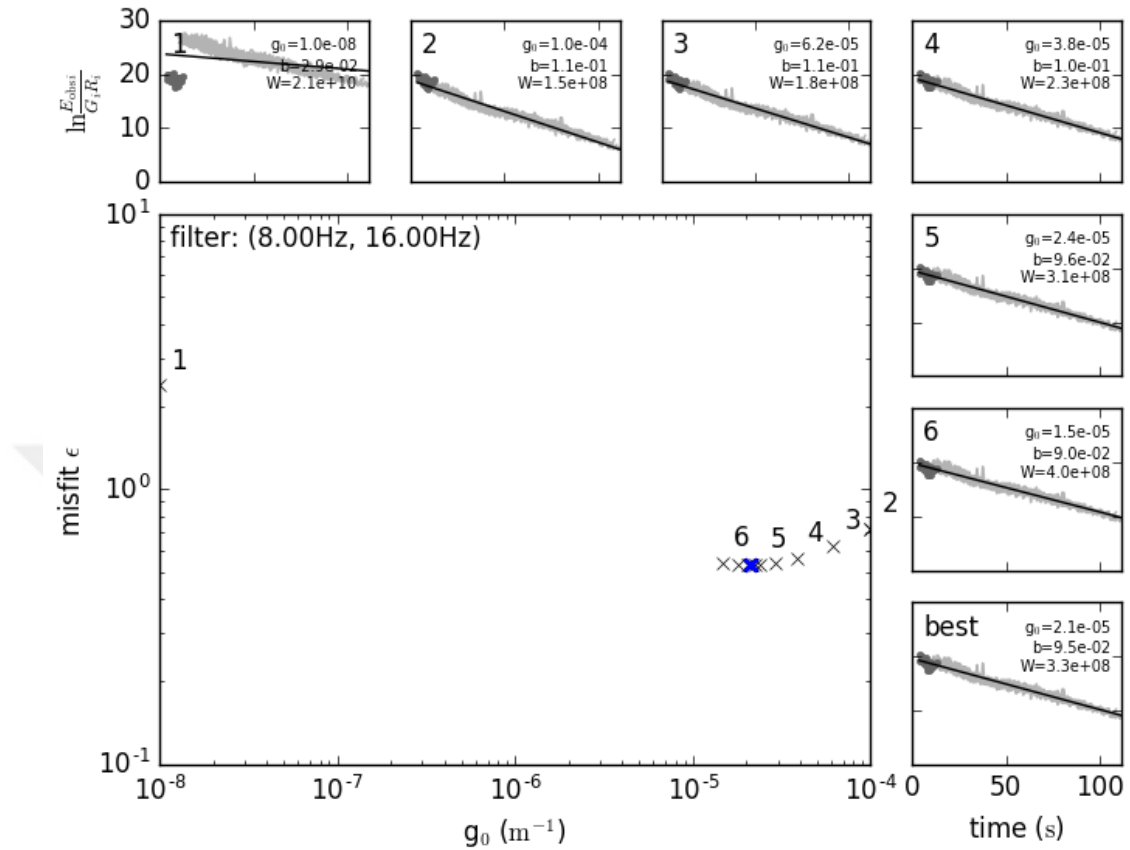


Figure 4.1. Optimization with error function is given for one event (20120707070746) observed in 22 stations in 8-16 Hz frequency band. The big panel refers to the optimization and blue cross is the point where $g^* = g_0$. Remaining small panels, the least square solutions are represented in 6 guesses and one best solution in lower right-hand sided panel where grey curves and dots are the observed envelopes of coda and direct S-wave. The best guess represents the best value of g_0 with low misfit.

4.2. Estimation of Source Parameters

Seismic moment M_0 is related to the physical properties of a seismic source and hence it is used for quantification for the magnitude of an earthquake. It can be considered as the driving force that has a particular direction in 3D space and give rises to the movement oriented with its own direction on 2D fault plane. This makes the determining of seismic moment difficult, as the first order approximation earth scientists utilize scalar moment in magnitude estimations.

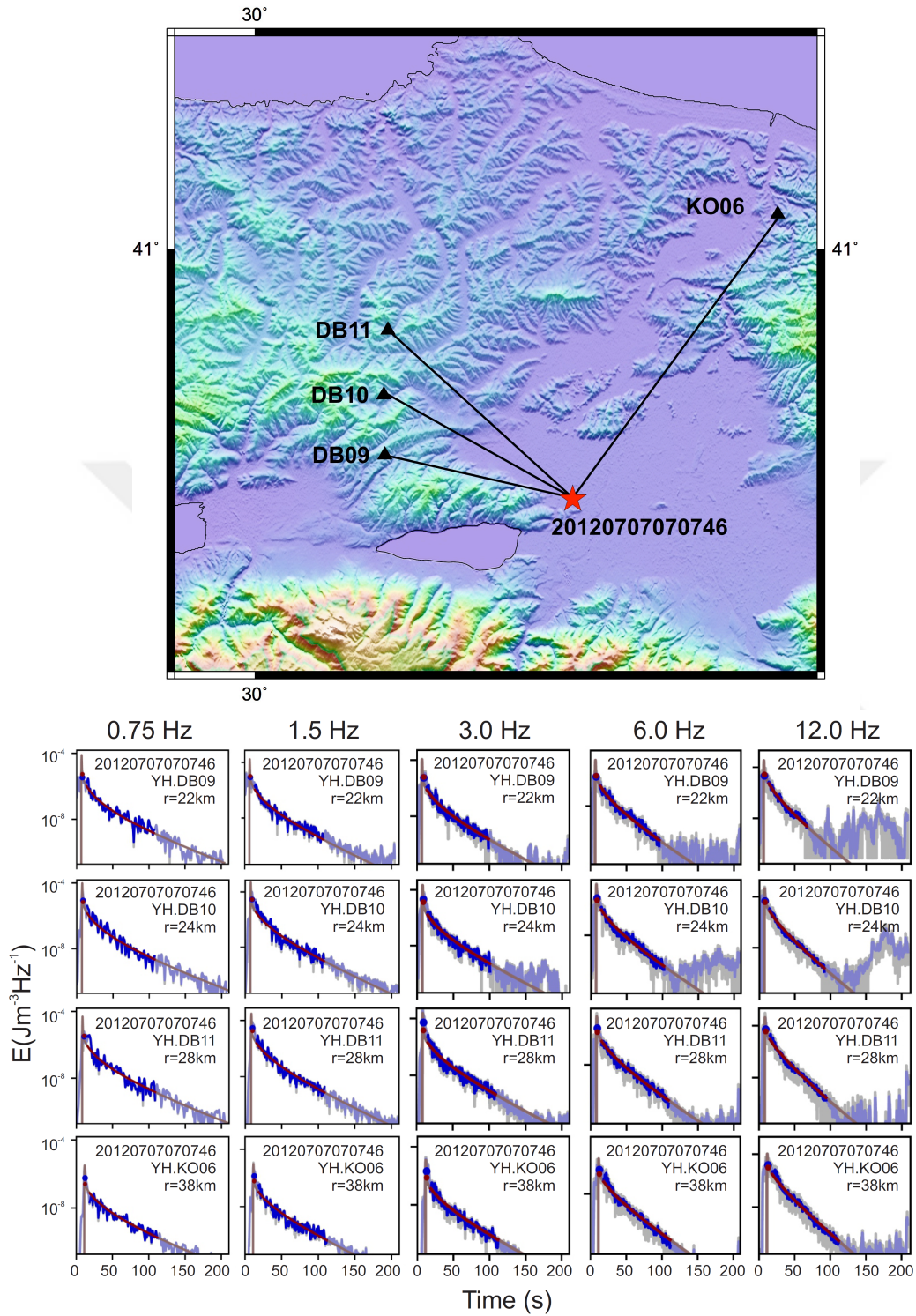


Figure 4.2. Example fits between observed and modeled envelopes for a specific event (red star on the map) recorded at four stations (black triangles on the map) are shown for five frequency bands. Observed raw and smoothed envelopes are represented by grey and blue color, respectively. Red decaying curve indicates synthetic envelope computed for optimal parameters reached at the end of inversion process.

Mechanical process taking place during an earthquake can be expressed by scalar seismic moment as the energy released with earthquake is strongly related to the interaction between the opposite block of the crust on a fault. Thus scalar seismic moment can be approximately estimated from field observations by:

$$M_0 = \mu \cdot u \cdot A \quad (4.6)$$

where μ corresponds to the S-wave resistance as a material strength while u is average fault displacement and A indicates the rupture area. According to Hanks & Thatcher (1972), seismic moment can be calculated with spectral amplitude as presented in equation 4.7.

$$M_0 = 4\pi\rho V_s^3 \Delta \Omega_0 \quad (4.7)$$

In equation 4.7, ρ represents rock density, V_s is S-wave velocity, Δ is hypocentral distance and Ω_0 is spectral level of long period shear waves.

In the present work, simultaneous inversion process (Eulenfeld and Wegler, 2016) resulted in calculated frequency dependency of spectral source energy W . This information was used to generate source displacement spectrum which could be later used for seismic moment, M_0 and moment magnitude, M_w calculations.

As Sato et al. (2012) stated the S-wave source displacement spectrum can be estimated by using following equation:

$$\omega M(f) = \sqrt{\frac{5\rho_0 v_0^5 W}{2\pi f^2}} \quad (4.8)$$

In Abercrombie (1995) the relation between source displacement spectrum and seismic moment M_0 and corner frequency f_c is described by:

$$\omega M(f) = M_0 \left(1 + \left(\frac{f}{f_c}\right)^\gamma\right)^{-\frac{1}{\gamma}} \quad (4.9)$$

In equation 4.9, γ indicates the sharpness of transition from a constant level of seismic moment at low frequencies to the decrease with f^{-n} at high frequencies. n is the high frequency fall-off (Eulenfeld & Wegler, 2016).

Taking the natural logarithms of every term in equation 4.9 will yield:

$$\ln \omega M(f) = \ln M_0 - \frac{1}{\gamma} \ln \left(1 + \left(\frac{f}{f_c}\right)^\gamma\right) \quad (4.10)$$

Equation 4.10 implies that the observed source displacement spectrum, $ln\omega M(f)$ can be inverted simultaneously for seismic moment, corner frequency, sharpness and high frequency fall-off. The illustration of this procedure for an earthquake can be seen in Figure 4.3.

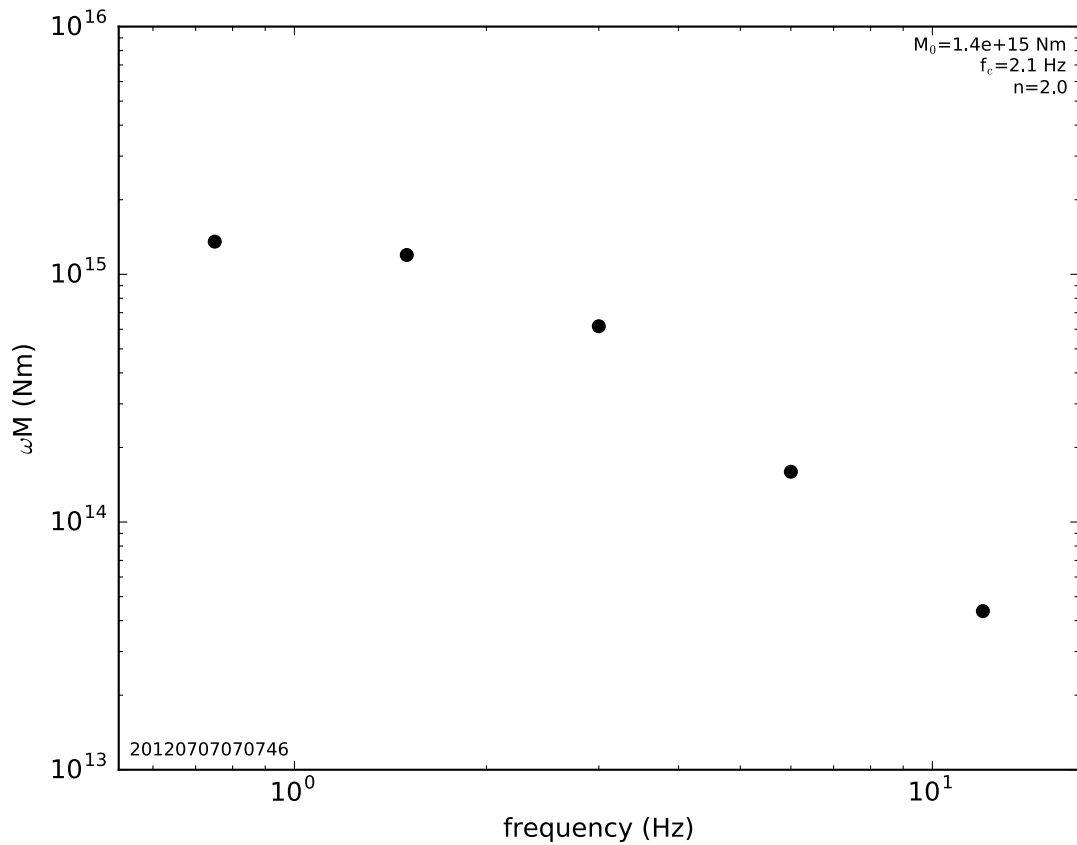


Figure 4.3. Illustration of inversion for source parameters of an earthquake (201207070746).

Although seismic moment is the best illustration of sizing an earthquake source its usage in practice is difficult since it can take very large values. Thus seismologists prefer to use moment magnitude, M_w , another quantity that is estimated from seismic moment and also directly related to the size of earthquake source. Following empirical relation that is given in Hanks & Kanamori (1979) was used to calculate M_w :

$$M_w = \frac{2}{3} \log_{10} M_0 - 6.07 \quad (4.11)$$

5. RESULTS AND INTERPRETATIONS

5.1. Structural Parameters

In this thesis, we successfully applied an inversion technique to estimate 2D lateral variations of intrinsic and scattering attenuation resulting in with characterization of crustal variations in relation with geological background. In general, Q_i^{-1} , Q_s^{-1} , and Q_t^{-1} calculations are in accordance with early coda studies that have aimed at imaging frequency-dependent attenuation variation of coda waves at different tectonic settings (e.g. Sens-Schönfelder & Wegler, 2006; Gaebler et al., 2015b; Eulenfeld & Wegler, 2016, 2017). In sections 5.1.1 and 5.1.2 we present values of Q_i^{-1} , Q_s^{-1} , and Q_t^{-1} by 2D lateral variations and comparison of the variation of attenuation values among northern, middle and southern parts of the study area, respectively.

5.1.1. 2D lateral variations of attenuation

In this section we present the calculations of inverse of intrinsic, scattering and total quality factors in 2D. Our motivation was to discover the dominant attenuation type on total attenuation at varying frequencies. Ductile deformation exhibits strong intrinsic attenuation, whereas scattering attenuation is mostly an evidence for brittle deformation. According to our calculations the inverse of scattering quality factor Q_s^{-1} ranges from 0.00013 at 12 Hz to 0.06347 at 0.75 Hz while the inverse of intrinsic quality factor Q_i^{-1} varies from 0.00095 at 12 Hz to 0.0227 at 0.75 Hz frequency bands. Total attenuation of seismic waves, the sum of inverse of intrinsic and scattering quality factors, Q_t^{-1} were determined as 0.001446 at 12 Hz to 0.08597 at 0.75 Hz. Detailed results of intrinsic, scattering and total quality factors are given in Table 5.1.

These calculation results could also be seen in Figure 5.1, which presents the 2D lateral variations. The northern and southern strands are clearly marked by attenuation properties at various frequencies. Domination of the attenuation type, which is also an indicator of the deformation type, varies on different frequency bands.

Intrinsic attenuation appears to be dominant for higher frequencies (6 Hz and 12 Hz), whereas the scattering attenuation controls the attenuating behaviour at lower frequencies (0.75, 1.5 and 3 Hz). These results were suggesting that small scale heterogenities are located at deeper parts of the upper crust while mineral dislocations or heat source presents at shallower parts beneath the western part of NAFZ.

Table 5.1: Minimum and maximum calculated values of Q_i^{-1} , Q_s^{-1} , Q_t^{-1} at five different frequency bands.

Q type \ Frequency	Q_i^{-1}		Q_s^{-1}		Q_t^{-1}	
	Min.	Max.	Min.	Max.	Min.	Max.
0.75 Hz	0.00643	0.02270	0.00776	0.06347	0.01561	0.08597
1.5 Hz	0.006663	0.013395	0.004801	0.014139	0.01191	0.02632
3.0 Hz	0.002977	0.006957	0.000897	0.002570	0.004492	0.00926
6.0 Hz	0.001592	0.003777	0.000183	0.002361	0.002186	0.00593
12 Hz	0.000953	0.003007	0.000131	0.002197	0.001446	0.00493

5.1.2. Comparison among different tectonic units

Apart from the lowest frequency 0.75 Hz which is suggest that the area between two strands presents higher attenuation for Q_i^{-1} , Q_s^{-1} , and Q_t^{-1} , overall results implies that attenuation values are getting stronger towards southern parts. To show the results explicitly we present a comparison of attenuation parameters among northern, southern and middle parts versus frequency in Figure 5.2. From 0.75 Hz to 12 Hz Q_i^{-1} varies between 0.007 and 0.001 for the northern part, 0.014 and 0.003 for middle part, lastly 0.010 and 0.002 for the southern part respectively. While, Q_s^{-1} changes from 0.015 to 0.001 for northern part and from 0.038 to 0.001 for middle, 0.014 to 0.001 for southern part. In total, attenuation results are in the range of 0.023 in 0.75 Hz band to 0.001 in 12 Hz frequency band for northern, from 0.051 at 0.75 Hz to 0.002 at 12 Hz for the middle and from 0.025 in 0.75 Hz up to 0.003 in 12 Hz for the southern part respectively. To better describe the attenuation at northern, southern and middle part, we applied best fitting power law. The frequency dependence of the total attenuation follows this power law given in Table 5.2.

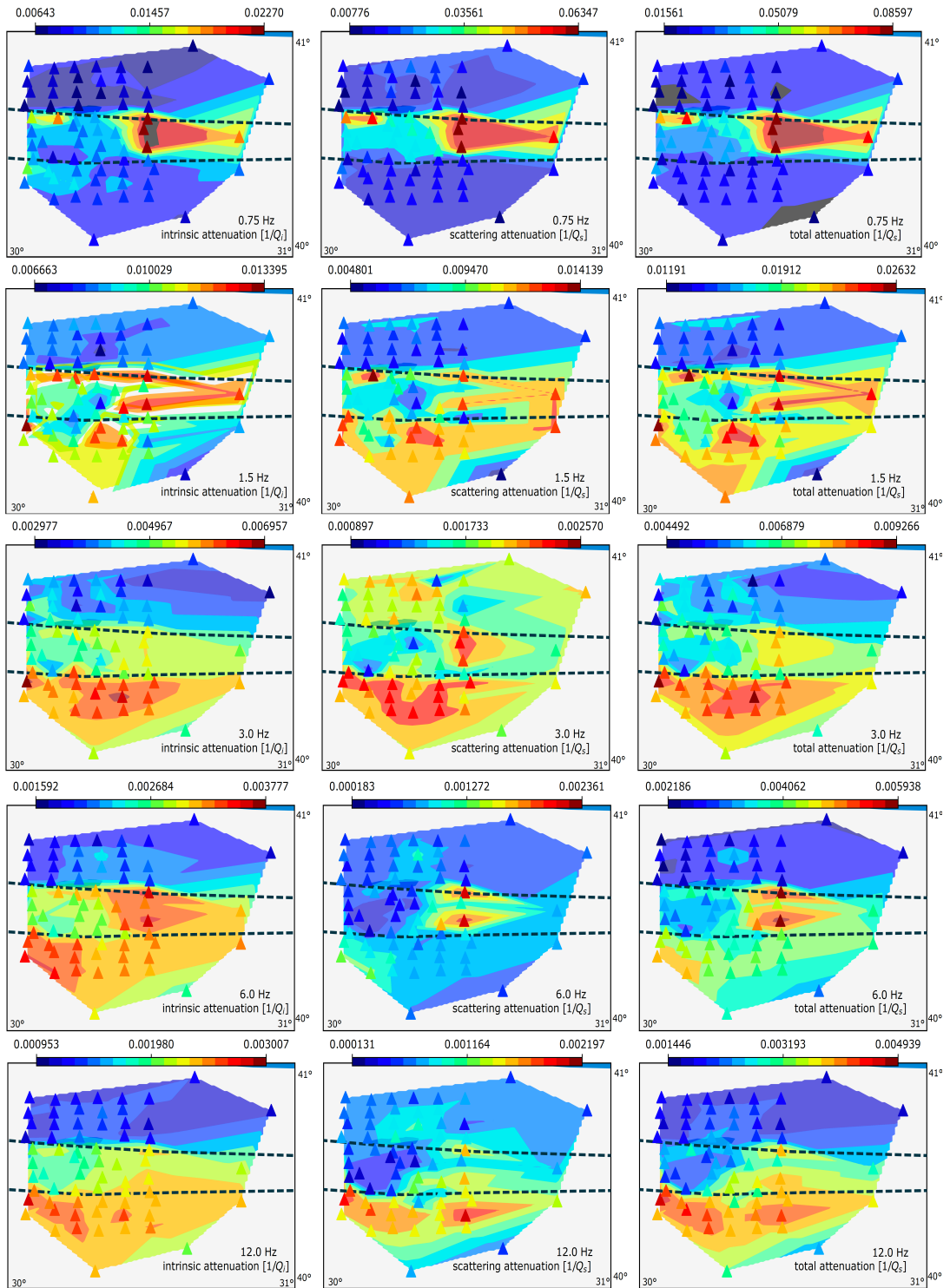


Figure 5.1. 2-D variation of the inverse of the quality factors (Q_i^{-1} , Q_s^{-1} , Q_t^{-1}) that represent seismic intrinsic (left), scattering (middle) and total attenuation (right) parameters in the study area for investigated frequency bands (increasing from top to bottom). Blueish colors mean weaker attenuation while reddish colors indicate stronger attenuation. Triangles show the station location and color coded by the corresponding attenuation values. Attenuation values between stations are interpolated.

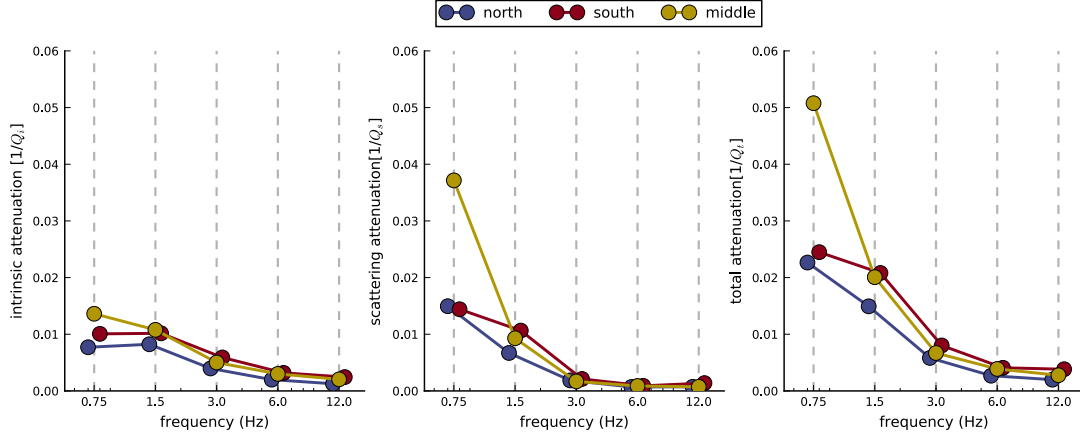


Figure 5.2. Inverse of the quality factors (Q_i^{-1} , Q_s^{-1} , Q_t^{-1}) that vary with frequency in the northern (blue), southern (red) and middle (yellow) region of the western part of the NAFZ.

Table 5.2: Best-fitting power laws for total attenuation Q_t^{-1} as a function of frequency.

Location	Power law for Q_t^{-1}
Istanbul-Zonguldak zone	$0.018 \times f^{-0.82}$
Armutlu-Almacık zone	$0.034 \times f^{-1.25}$
Sakarya zone	$0.021 \times f^{-0.66}$

There are several studies which have similar results with ours and our results suggests firstly that, Istanbul-Zonguldak Zone is characterized by overall low intrinsic and low scattering parameters whereas the Sakarya Zone to the south displays an opposite pattern. For instance, Tank et al. (2005) modeled electromagnetic data and Ateş et al. (1999) modeled gravity measurements and elucidated a large, dense and highly resistive structure down to 10 km beneath the Istanbul zone which is quite coherent with our result which are showing relatively low attenuation behaviour in Istanbul zone. Furthermore, Yiğitbaş et al. (2004) revealed, relatively high P and S-wave speeds in Istanbul zone and suggests the presence of an ancient and strong crystalline basement which supports our results. This may evidence for sharp differences in variation of both type attenuation parameters at all frequency bands.

Unlike the Istanbul Zone, we observed high intrinsic and scattering attenuation beneath the Sakarya Zone which is in a good agreement with relatively low S-wave velocities and high $\delta(V_P/V_S)$ reported by Papaleo et al. (2017, 2018) for the upper crust down to 15 km depth. Papaleo et al. (2017, 2018) also stated that the differences on P and S-

wave velocities within the crust and uppermost mantle and they concluded that significant contrasts in V_p/V_s ratio would result from the juxtaposition between the Armutlu Peninsula with Triassic–Cretaceous tectonic aggregates (Yılmaz & Tüysüz, 1997) and the Istanbul Zone accommodating a Proterozoic granitic and metamorphic basement underlying Ordovician to Carboniferous age sedimentary sequences (Chen et al., 2002).

The Armutlu-Almacık in between is more complex with low-to-high locally varying attenuating pattern from west to east which is consistent with inverse modeling of local earthquake data estimated by Koulakov et al. (2010). Armutlu-Almacık zone is a narrow but complex domain which consists Triassic subduction/accretion units and Jurassic-Eocene sedimentary sequences from Sakarya zone and also Cretaceous-Palaeocene complex and metamorphic rocks with unknown origin and age (e.g. Şengör & Yılmaz, 1981; Okay et al., 2008). In relation with suggestions of Eulenfeld & Wegler (2016) as the stepwise decreasing of attenuation parameters are because of the change in lithology from crystalline basin to sedimentary rocks, we relate the relatively low attenuation values in the east of Armutlu-Almacık zone, for higher frequencies, to the existing pre-Jurassic basement Lower Cretaceous complex and metamorphic rocks of Istanbul zone. However, we observe an increase in attenuation values in the west of Armutlu-Almacık zone, which corresponds to the Kuzuluk Basin. The sedimentary Kuzuluk Basin was formed as a result of opening pull-apart zone and east-west extensional regime that was confirmed by Koulakov et al. (2010). Additionally, as positive temperature anomalies estimated by Ilişik, 1995 and presence of thermal activities revealed (e.g., Greber, 1994), indicating that an active pull-apart extension exists.

Several lithological contrasts have shown as a result of the progressive displacement of NAFZ. As a result of 900 km rupture of NAFZ in the twentieth century a long term relative motion of crustal blocks have been noticed along the faults which explains the contrasts in attenuation values. Similar to aforementioned results with contrasts of crustal properties, there are several seismological models as 3-D seismic tomography (e.g. Yolsal-Çevikbilen et al., 2012; Fichtner et al., 2013a,b; Delph et al., 2015; Çubuk-Sabuncu et al., 2017), receiver functions studies (e.g. Frederiksen et al., 2015; Kahraman et al., 2016), fault-guided head wave analyses (Bulut et al., 2012; Najdahmadi et al., 2016), by 2D/3D geoelectric methods (Kaya et al., 2013 and references therein).

5.2. Magnitude Estimates

In addition to the attenuation parameters, as a bi-product of the inversion we estimated moment magnitudes M_w for each individual earthquake in our dataset. Figure 5.3, shows a scatter plot between coda-derived magnitudes and the catalog magnitudes based on a local magnitude scale M_L . In general, there is a good agreement between our estimates and catalog magnitudes. Also a move-out can be observed that is likely caused by using different scales for magnitude comparison. Our non-empirical coda envelope fitting approach can be considered successful mostly for the magnitudes greater than 3.0. For the magnitudes less than 2.5 M_w , large scatters occurred which can be explained by wrongly estimated magnitudes and small errors during the inversion process while calculating the other parameters on quality factors of intrinsic and scattering attenuation. There are several studies to estimate coda derived magnitudes and our results are similarly consistent with them. For instance, Mayeda et al. (2005) and Phillips et al. (2014) studied coda waves with 2D path corrected stations and estimated source parameters, which are coherent with regional moment tensor solutions for the same earthquakes. Moreover, a similar type of consistency has been earlier reported in Eken et al. (2004) and Gök et al. (2016) who utilized empirical coda waves approach assuming a simple 1-D radially symmetric path correction in Turkey.

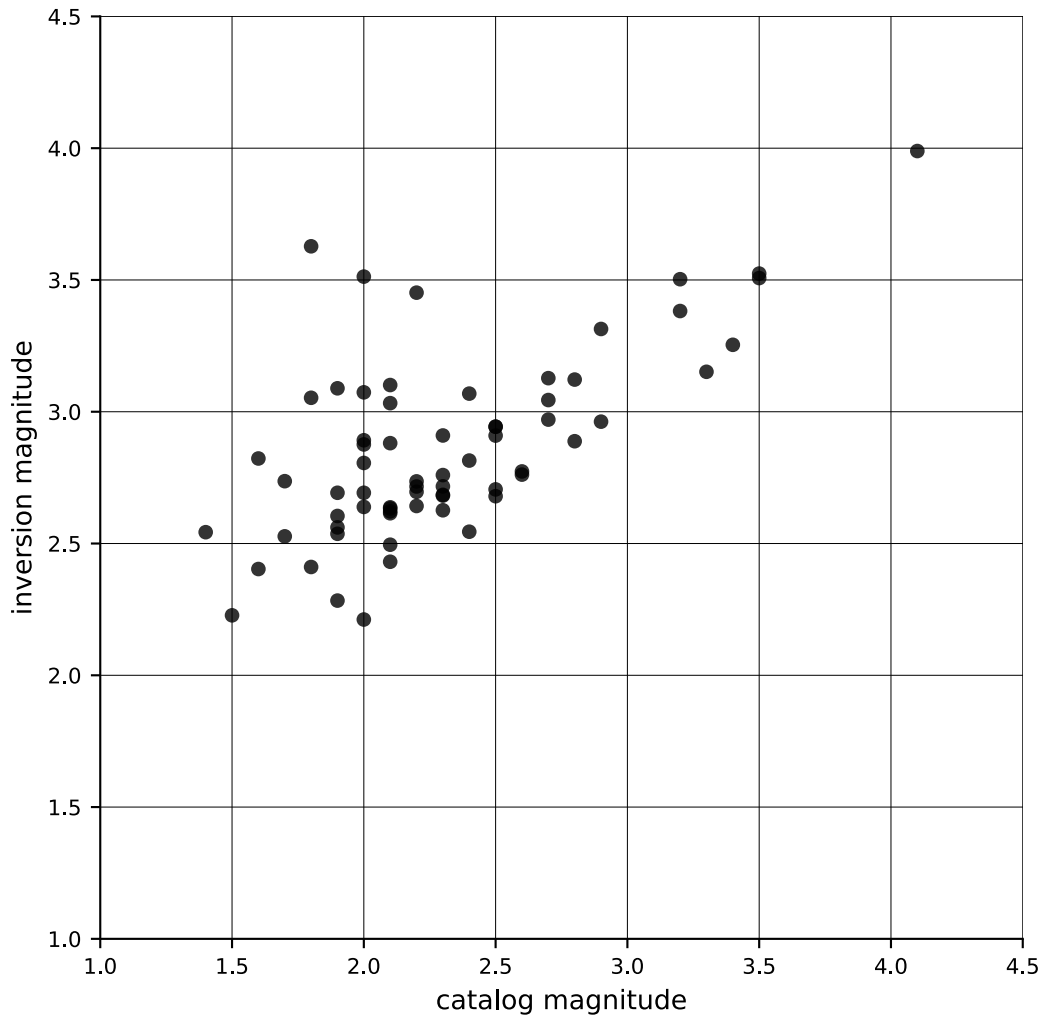


Figure 5.3. Comparison between catalog magnitudes of local events with those derived from coda waves as a side product of the inversion process.



6. CONCLUSION

In this thesis, we present estimates of intrinsic and scattering attenuation properties of the crust in a frequency scale from 0.75 to 12.0 Hz using local earthquakes in the western part of NAFZ. We applied acoustic radiative transfer theory under the assumption of multiple isotropic media to separate intrinsic and scattering attenuation parameters. The good fits between observed and synthetic envelopes have shown that, this method is reliably working even in this tectonically active and complex regime. We provide 2D spatial distribution of intrinsic and scattering attenuation in the study area which revealed that scattering attenuation is dominant over intrinsic in deeper portions of the crust (frequencies at 0.75, 1.5 and 3.0 Hz) while in shallower parts which corresponds to the higher frequencies as 6.0 and 12.0 Hz intrinsic attenuation becomes dominant. Apart from these, the spatial variation of attenuative behaviour increases from the Istanbul-Zonguldak zone at the northern, to Sakarya zone in the south. This increase corresponds to the lithological difference between those tectonic units. Particularly, very high attenuation values is observed over Kuzuluk Basin which is a pull-apart basin formed due to west-east extension which corresponds to the western part of Armutlu-Almacık zone. Attenuation values from east to west within Armutlu-Almacık zone due to its complexity.

Since our approach yields source displacement spectrum we were able to calculate the moment magnitudes (M_w) for each earthquake. As a bi-product of this study, we provide coda derived moment magnitudes for each individual earthquake in our dataset which have shown a good agreement with the local magnitudes from the earthquake catalog. Generally, our results are consistent with previous geophysical and geological studies over the study region even in this tectonically complex regime which implies our non-empirical inversion approach is successful.

To conclude, we applied acoustic radiative transfer theory under the assumption of multiple isotropic scattering and we provide an accurate application of this inversion approach in western part of NAFZ which is tectonically complex and laterally heterogeneous region. Additionally we provide coda derived M_w for each individual earthquake in our dataset. This thesis covers a small region of Anatolian Plate with

continuously deforming nature. A further work can be accomplished to highlight the crustal structure beneath the Anatolian Plate and the adjacent areas.



REFERENCES

- Abercrombie, R.E.** (1995). Earthquake source scaling relationships from -1 to $5 M_L$ using seismograms recorded at 2.5-km depth. *J. Geophys. Res. Solid Earth.*, 100, 24,015-24,036.
- Abubakirov, I.R. & Gusev, A.A.** (1990). Estimation of scattering properties of lithosphere of Kamchatka based on Monte-Carlo simulation of record envelope of a near earthquake. *Phys. Earth Planet. Inter.*, 64, 52-67.
- Aki, K.** (1969) Analysis of the seismic coda of local earthquakes as scattered waves. *J. Geophys. Res.* 74(2), 615–631.
- Aki, K. & Chouet, B.** (1975). Origin of coda waves: Source, attenuation, and scattering effects. *J. Geophys. Res.* 80(23), 3322–3342.
- Altuncu Poyraz, S., Teoman, M.U., Türkelli, N., Kahraman, M., Cambaz, D., Mutlu, A., Rost, S., et al.** (2015). New constraints on micro-seismicity and stress state in the western part of the North Anatolian Fault Zone: Observations from a dense seismic array. *Tectonophysics.* 656, 190-201.
- Ates, A., Kearey, P. & Tufan, S.** (1999). New gravity and magnetic anomaly maps of Turkey. *Geophys. J. Int.* 136, 499-502
- Barka, A.A.** (1992). The north Anatolian fault zone. *Ann. Tectonicae.* 6, 164-195.
- Barka, A.A.** (1996). Slip distribution along the North Anatolian fault associated with the large earthquakes of the period 1939 to 1967. *Bull. Seismol. Soc. Am.*, 86, 1238–1254.
- Barka, A.A. & Kadinsky- Cade, K.** (1988). Strike- slip fault geometry in Turkey and its influence on earthquake activity. *Tectonics.*, 7(3), 663–684.
- Bayrakci, G., Laigle, M., Bécel, A., Hirn, A., Taymaz, T., Yolsal-Çevikbilen, S., SEISMARMARA team** (2013). 3-D sediment-basement tomography of the Northern Marmara trough by a dense OBS network at the nodes of a grid of controlled source profiles along the North Anatolian fault, *Geophys. J. Int.*, 194, 1335–1357.
- Bianco, F., Pezzo, E. Del, Castellano, M., Ibanez, J. & Luccio, F. Di.** (2002) Separation of intrinsic and scattering seismic attenuation in the Southern Apennine zone, Italy. *Geophys. J. Int.*, 150, 10-22.

- Beyreuther, M., Barsch, R., Krischer, L., Megies, T., Behr, Y. & Wassermann, J.** (2010). ObsPy: A Python Toolbox for Seismology. *Seismol. Res. Lett.*, 81, 530-533.
- Bohnhoff, M., Kwiatek, G., Martinez-Garcon, P. & Dresen, G.** (2013). Microseismic monitoring of reservoir stimulation: Case studies and implications for improved geomechanical characterization. *75th EAGE Conf. Exhib. Inc. SPE Eur. 2013*.
- Bulut, F., Ben-Zion, Y. & Bohnhoff, M.** (2012). Evidence for a bimaterial interface along the Mudurnu segment of the North Anatolian Fault Zone from polarization analysis of P waves. *Earth Planet. Sci. Lett.*, 327-328, 17-22.
- Canas, J.A., Ugalde, A., Pujades, L.G., Carracedo, J.C., Soler, V. & Blanco, M.J.** (1998). Intrinsic and scattering seismic wave attenuation in the Canary Islands. *J. Geophys. Res.*, 103(7), 15037-15050
- Chandrasekhar, S.**, (1960) Radiative Transfer, Dover Publications, Inc.
- Chen, F., Siebel, W., Satir, M., Terzioglu, M. & Saka, K.** (2002). Geochronology of the Karadere basement (NW Turkey) and implications for the geological evolution of the Istanbul zone. *Int. J. Earth Sci.*, 91, 469.
- Çubuk-Sabuncu, Y., Taymaz, T. & Fichtner, A.** (2017). 3-D crustal velocity structure of western Turkey: Constraints from full-waveform tomography. *Phys. Earth Planet. Inter.*, 270, 90-112.
- DANA** (2012). Dense Array for North Anatolia. International Federation of Digital Seismograph Networks. Other/Seismic Network. 10.7914/SN/YH_2012.
- Dainty, A.M., Toksöz, M.N., Anderson, K.R., Pines, P.J., Nakamura, Y. & Latham, G.** (1974). Seismic scattering and shallow structure of the moon in oceanus procellarum. *The Moon.*, 9, 11-29.
- Delph, J.R., Zandt, G. & Beck, S.L.** (2015). A new approach to obtaining a 3D shear wave velocity model of the crust and upper mantle: An application to eastern Turkey. *Tectonophysics.*, 665, 92-100.
- Dewey, J.F. & Şengör, A.M.C.** (1979). Aegean and surrounding regions: Complex multiplate and continuum tectonics in a convergent zone. *Bull. Geol. Soc. Am.* 90 (1), 84-92.
- Duman, T.Y., Emre, O., Dogan, A. & Ozalp, S.** (2005). Step-over and bend structures along the 1999 Duzce earthquake surface rupture, North Anatolian Fault, Turkey. *Bull. Seismol. Soc. Am.*, 95 (4), 1250-1262.
- Eken, T., Mayeda, K., Hofstetter, A., Gök, R., Orgülü, G. & Turkelli, N.** (2004). An application of the coda methodology for moment-rate spectra using broadband stations in Turkey. *Geophys. Res. Lett.*, 31, L11609.

- Elmas, A. & Gürer, A.** (2004). A comparison of the geological and geoelectrical structures in the Eastern Marmara region (NW Turkey). *J. Asian Earth Sci.*, 23, 153-162.
- Emoto, K., Sato, H. & Nishimura, T.**, (2010). Synthesis of vector wave envelopes on the free surface of a random medium for the vertical incidence of a plane wavelet based on the Markov approximation, *J. geophys. Res.*, 115, 1–15.
- Eulenfeld, T. & Wegler, U.** (2017). Crustal intrinsic and scattering attenuation of high-frequency shear waves in the contiguous United States. *J. Geophys. Res. Solid Earth*. 122, 4676–4690.
- Eulenfeld, T. & Wegler, U.** (2016). Measurement of intrinsic and scattering attenuation of shear waves in two sedimentary basins and comparison to crystalline sites in Germany. *Geophys. J. Int.*, 205, 744–757.
- Fichtner, A., Kennett, B.L.N. & Trampert, J.** (2013). Separating intrinsic and apparent anisotropy. *Phys. Earth Planet. Inter.*, 219,11-20.
- Fichtner, A., Trampert, J., Cupillard, P., Saygı, E., Taymaz, T., Capdeville, Y., & Villasenor, A.** (2013). Multiscale full waveform inversion. *Geophys. J. Int.*, 194, 534-556.
- Frankel, A. & Wennerberg, L.** (1987). Energy-flux model of seismic coda: Separation of scattering and intrinsic attenuation. *Bull. Seism. Soc. Am.*, 77,1223-1251
- Frederiksen, A.W., Thompson, D.A., Rost, S., Cornwell, D.G., Gülen, L., Houseman, G.A., Kahraman, M., et al.** (2015). Crustal thickness variations and isostatic disequilibrium across the North Anatolian Fault , western Turkey, *Geophys. Res. Lett.*, 42, 751–757.
- Gaebler, P.J.**, (2015). The Influence of Crustal Heterogeneity on Translational and Rotational Motions in the Seismic Coda (Doctoral Dissertation), University of Leipzig.
- Gaebler, P.J., Eulenfeld, T. & Wegler, U.** (2015). Seismic scattering and absorption parameters in the W-Bohemia/Vogtland region from elastic and acoustic radiative transfer theory. *Geophys. J. Int.* 203, 1471-1481.
- Gaebler, P.J., Sens-Schönfelder, C. & Korn, M.** (2015). The influence of crustal scattering on translational and rotational motions in regional and teleseismic coda waves. *Geophys. J. Int.*, 201, 355-371.
- Gaebler, P.J., Eken, T., Bektaş, H.Ö., Eulenfeld, T., Wegler, U. & Taymaz, T.** (2018). Imaging of Shear Wave Attenuation Along the Central Part of the North Anatolian Fault Zone, Turkey. *J. Seismol.* (Under Review)

- Goldstein, P., Dodge, D., Firpo, M. ve Stan, R.** (1998). Electronic Seismologist: What's new in SAC 2000 Enhanced Processing ve Database Access. *Seismol. Res. Lett.*, 69, 202–205.
- Gök, R., Kaviani, A., Matzel, E.M., Pasyanos, M.E., Mayeda, K., Yetirmishli, G., Hussain, I. El, et al.** (2016). Moment magnitudes of local/regional events from 1D coda calibrations in the broader middle east region. *Bull. Seismol. Soc. Am.* 106 (5), 1926-1938.
- Greber, E.** (1994). Deep circulation of CO₂-rich palaeowaters in a seismically active zone (Kuzuluk/ Adapazari, Northwestern Turkey). *Geothermics*. 23(2), 151-174.
- Greber, E.** (1997). Stratigraphic evolution and tectonics in an area of high seismicity: Akyazi/Adapazari (Pontides, Northwestern Turkey). In Schindler, C. & Pfister, M., (Eds.) *Active Tectonics of Northwestern Anatolia-The Marmara Poly-Project*. (pp. 141-155) ISBN: 3 7281 2425 7
- Gusev, A. A., & Lemzikov, V. K.** (1985). Properties of scattered elastic waves in the lithosphere of Kamchatka: Parameters and temporal variations, *Tectonophysics*, 112, 137-153.
- Hanks, T.C. & Kanamori, H.** (1979). A moment magnitude scale. *J. Geophys. Res. B Solid Earth*. 84(B5), 2348–2350.
- Hanks, T.C. & Thatcher, W.** (1972). A graphical representation of seismic source parameters. *J. Geophys. Res.* 77, 4393-4405
- Hoshiya, M.** (1993). Separation of scattering attenuation and intrinsic absorption in Japan using the multiple lapse time window analysis of full seismogram envelope. *J. Geophys. Res.*. 98(B9), 15809–15824
- Hoshiya, M.** (1997) Seismic coda wave envelope in depth-dependent S wave velocity structure. *Phys. Earth Planet. Inter.*, 104, 15-22.
- Houseman, G.A.** (2017). Why Earthquakes Threaten Two Major European Cities: Istanbul and Bucharest. *Eur. Rev.*, 26, 30-49.
- Ilkişik, O.M.** (1995). Regional heat flow in western Anatolia using silica temperature estimates from thermal springs. *Tectonophysics*. 244, 175-184.
- Jin, A., and Aki, K.** (1989). Spatial and temporal correlation between coda Q¹ and seismicity and its physical mechanism, *J Geophys. Res.*, 94, 14041-14059.
- Kahraman, M., Cornwell, D.G., Thompson, D.A., Rost, S., Houseman, G.A., Türkelli, N., Teoman, U., et al.** (2015). Crustal-scale shear zones and heterogeneous structure beneath the North Anatolian Fault Zone, Turkey, revealed by a high-density seismometer array. *Earth Planet. Sci. Lett.*, 430, 129–139.

- Karabulut, H., Roumelioti, Z., Benetatos, C., Mutlu, A.K., Özalaybey, S., Aktar, M. & Kiratzi, A.** (2006) A source study of the 6 July 2003 (Mw5.7) earthquake sequence in the Gulf of Saros (Northern Aegean Sea): Seismological evidence for the western continuation of the Ganos fault. *Tectonophysics*. 412, 195-216.
- Kaya, T., Tank, S.B., Tunçer, M.K., Rokoityansky, I.I., Tolak, E. & Savchenko, T.** (2009) Asperity along the north anatolian fault imaged by magnetotellurics at Düzce, Turkey. *Earth, Planets Sp.*, 61, 871–884.
- Kaya, T., Kasaya, T., Tank, S.B., Ogawa, Y., Tunçer, M.K., Oshiman, N., Honkura, Y., et al.** (2013) Electrical characterization of the north anatolian fault zone underneath the marmara sea, turkey by ocean bottom magnetotellurics. *Geophys. J. Int.*, 193, 664–677.
- Ketin, I.** (1966), Tectonic Units of Anatolia, MTA, 66, 23-34.
- Kondo, H., Awata, Y., Emre, Ö., Doğan, A., Özalp, S., Tokay, F., Yildirim, C., et al.** (2005) Slip distribution, fault geometry, and fault segmentation of the 1944 Bolu-Gerede earthquake rupture, North Anatolian fault, Turkey. *Bull. Seismol. Soc. Am.*, 95 (4), 1234-1249.
- Kondo, H., Özaksoy, V. & Yildirim, C.** (2010) Slip history of the 1944 Bolu-Gerede earthquake rupture along the North Anatolian fault system: Implications for recurrence behavior of multisegment earthquakes. *J. Geophys. Res. Solid Earth*. 115, B04316.
- Koulakov, I., Bindi, D., Parolai, S., Grosser, H. & Milkereit, C.** (2010) Distribution of Seismic Velocities and Attenuation in the Crust beneath the North Anatolian Fault (Turkey) from Local Earthquake Tomography. *Bull. Seismol. Soc. Am.*, 100, 207–224.
- Koyanagi, S., Mayeda, K. & Aki, K.** (1992). Frequency-dependent site amplification factors using the S-wave coda for the Island of Hawaii, *Bull. Seism. Soc. Am.*, 82, 1151-1185
- Mayeda, K. & Walter, W.R.** (1996). Moment, energy, stress drop, and source spectra of western United States earthquakes from regional coda envelopes. *J. Geophys. Res. Solid Earth*. 101(B5), 11195–11208.
- Mayeda, K., Hofstetter, A., O'Boyle, J., Walter, W. R.** (2003). Stable and Transportable Regional Magnitudes Based on Coda-Depved Moment-Rate Spectra, *Bull. Seism. Soc. Am.*, 93, 224-239.
- McKenzie, D.** (1972). Active Tectonics of the Mediterranean Region. *Geophys. J. R. Astron. Soc.*, 30, 109-185.
- McClusky, S., Balassanian, S., Barka, A., Demir, C., Ergintav, S., Georgiev, I., Gurkan, O., et al.** (2000). Global Positioning System constraints on

plate kinematics and dynamics in the eastern Mediterranean and Caucasus. *J. Geophys. Res. Solid Earth*. 105(B3), 5695-5719.

Morse, P.M. and Feshbach, H. (1953) *Methods of Theoretical Physics*. McGraw-Hill Book Comp., Inc., New York, Toronto, London, Part I, Ch. 2, Paragraph 2.5, 208-209, 260.

Najdahmadi, B., Bohnhoff, M. & Ben-Zion, Y. (2016). Bimaterial interfaces at the Karadere segment of the North Anatolian Fault, northwestern Turkey. *J. Geophys. Res. Solid Earth*. 121, 931–950.

Nakamura, Y., (1977). Seismic energy transmission in an intensively scattering environment, *J. Geophys.*, 43, 389-399.

Nakamura, A., A. Hasegawa, A. Ito, S. B. Ucer, Ş. Baris, Y. Honkura, T. Kono, S. Hori, R. Pektaş, T. Komut, C. Celik, and A. M. Isikara (2002). P-wave velocity structure of the crust and its relationship to the occurrence of the 1999 Izmit, Turkey, earthquake and aftershocks, *Bull. Seismol. Soc. Am.* 92, 330–338

Okamoto, K., Mikada, H., Goto, T., Takekawa, J., (2013). Numerical analysis of the relationship between time-variant coda-Q and the variation in crustal stress *Geophys. J. Int.*, 195, 575-581.

Okay, A.I. & Tüysüz, O. (1999). Tethyan sutures of northern Turkey. *Geol. Soc. London, Spec. Publ.* 156, 475-515.

Okay, A.I., Bozkurt, E., Satir, M., Yiğitbaş, E., Crowley, Q.G. & Shang, C.K. (2008). Defining the southern margin of Avalonia in the Pontides: Geochronological data from the Late Proterozoic and Ordovician granitoids from NW Turkey. *Tectonophysics*. 461, 252-264.

Okay, A.I., Satir, M., Tüysüz, O., Akyüz, S. & Chen, F. (2001). The tectonics of the Strandja Massif: Variscan and mid-Mesozoic deformation and metamorphism in the northern Aegean. *International Journal of Earth Sciences*, 90, 217-233.

Paasschens, J. (1997). Solution of the time-dependent Boltzmann equation, *Phys. Rev. E*, 56(1), 1135–1141.

Papaleo, E., Cornwell, D.G. & Rawlinson, N. (2017). Seismic tomography of the North Anatolian Fault: New insights into structural heterogeneity along a continental strike-slip fault. *Geophys. Res. Lett.* 44, 2186–2193.

Papaleo, E., Cornwell, D. & Rawlinson, N. (2018) Constraints on North Anatolian Fault Zone Width in the Crust and Upper Mantle From S Wave Teleseismic Tomography. *J. Geophys. Res. Solid Earth.*, 123, 2908-2922.

Pasyanos, M.E., Gök, R. & Walter, W.R. (2016). 2D variations in coda amplitudes in the middle east. *Bull. Seismol. Soc. Am.*, 106 (5), 1915-1925.

- Polat, G., Özel, N.M. & Koulakov, I.** (2016). Investigating P- and S-wave velocity structure beneath the Marmara region (Turkey) and the surrounding area from local earthquake tomography the Next Marmara Earthquake: Disaster Mitigation, Recovery and Early Warning 4. Seismology. *Earth, Planets Sp.* 68, 132.
- Pucci, S., Pantosti, D., Barchi, M.R. & Palyvos, N.** (2007). A complex seismogenic shear zone: The Düzce segment of North Anatolian Fault (Turkey). *Earth Planet. Sci. Lett.* 262, 185-203.
- Ryzhik, L., Papanicolaou, G. & Keller, J.B.** (1996). Transport equations for elastic and other waves in random media. *Wave Motion.* 24, 327-370.
- Sato, H., Shomahmadov, A.M. , Khalturin, V.I. & Rautian, T. G.** (1988). Temporal change in spectral coda attenuation Q^{-1} associated with the $M=13.3$ earthquake of 1983 near Garm, Tadjikistan region in Soviet central Asia, *Zisin*, 41, 39-46.
- Sato, H., Fehler, M.C. & Maeda, T.,** (2012). Seismic Wave Propagation and Scattering in the Heterogeneous Earth, 2nd edn, Springer.
- Sens-Schönfelder, C. & Wegler, U.** (2006). Radiative transfer theory for estimation of the seismic moment. *Geophys. J. Int.* 167, 1363-1372.
- Sens-Schönfelder, C., Margerin, L., & Campillo, M.** (2009). Laterally heterogeneous scattering explains Lg blockage in the Pyrenees. *Journal of Geophysical Research: Solid Earth.* 114, B07309.
- Sertcelik, F. & Guleroglu M.** (2017). Coda Wave Attenuation Characteristics for North Anatolian Fault Zone, Turkey. *Open Geosci.*, 9,480–490.
- Stein, R.S., Barka, A.A. & Dieterich, J.H.** (1997). Progressive failure on the North Anatolian fault since 1939 by earthquake stress triggering. *Geophys. J. Int.* 128, 594-604.
- Sunal, G., Natalin, B., Satir, M. & Toraman, E.** (2006). Paleozoic magmatic events in the Strandja Masif, NW Turkey. *Geodinamica Acta* 19, 283-300.
- Şengör, A.M.C. & Yılmaz, Y.** (1981). Tethyan evolution of Turkey: A plate tectonic approach. *Tectonophysics.* 75, 181-241.
- Şengör, A.M., Tüysüz, O., İmren, C., Sakıncı, M., Eyidoğan, H., Görür, N., Pichon, X. Le, et al.** (2005). THE NORTH ANATOLIAN FAULT: A NEW LOOK. *Annu. Rev. Earth Planet. Sci.*, 33, 37-112.
- Tank, S.B., Honkura, Y., Ogawa, Y., Matsushima, M., Oshiman, N., Tunçer, M.K., Çelik, C., et al.** (2005). Magnetotelluric imaging of the fault rupture area of the 1999 Izmit (Turkey) earthquake. *Phys. Earth Planet. Inter.* 150, 213-225.

- Taymaz, T., Jackson, J. & Westaway, R.** (1990). Earthquake mechanisms in the Hellenic Trench near Crete. *Geophys. J. Int.*, 102, 695-731.
- Taymaz, T., Kasahara, J., Hirn, A. & Sato, T.** (2001). Investigations of MicroEarthquake Activity within the Sea of Marmara and Surrounding Regions by using Ocean Bottom Seismometers (OBS) and Land Seismographs: Initial Results, Scientific Activities 2001 Symposia Extended Abstracts Book, ISBN 975-97518-0-1.
- Taymaz, T., Westaway, R. & Reilinger, R.** (2004). Active faulting and crustal deformation in the Eastern Mediterranean region. *Tectonophysics*. 391,1-374.
- Taymaz, T., Yılmaz, Y. & Dilek, Y.** (2007). The geodynamics of the Aegean and Anatolia: introduction. *Geol. Soc. London, Spec. Publ.*
- Tsujiura, M.**, (1978). Spectral analysis of the coda waves from local earthquakes, *Bull. Earthq. Inst. Univ. Tokyo.*, 53, 1-48.
- Tucker, B., & King, J.** (1984). Dependence of sediment-filled valley response on input amplitude and valley properties, *Bull. Seism. Soc. Am.*, 74, 153-165.
- Ustaomer, T. & Robertson, A.H.F.** (2010). Late Palaeozoic-Early Cenozoic tectonic development of the Eastern Pontides (Artvin area), Turkey: stages of closure of Tethys along the southern margin of Eurasia. *Geol. Soc. London, Spec. Publ.* 340, 281-327.
- Vargas, C.A., Ugalde, A., Pujades, L.G. & Canas, J.A.** (2004). Spatial variation of coda wave attenuation in northwestern Colombia. *Geophys. J. Int.*, 158, 609-624.
- Warren, L.M., Beck, S.L., Biryol, C.B., Zandt, G., Ozacar, A. & Yang, Y.** (2013). Crustal velocity structure of Central and Eastern Turkey from ambient noise tomography. *Geophys. J. Int.*, 194, 1941-1654.
- Weber, M., Abu-Ayyash, K., Abueladas, A., Agnon, A., Al-Amoush, H., Babeyko, A., Bartov, Y., Baumann, M., Ben-Avraham, Z., Bock, G., Bribach, J., El-Kelani, R., Förster, A., Förster, H.-J., et al.** (2004). The crustal structure of the Dead Sea Transform, *Geophys. J. Int.*, 156, 655-681,
- Wilson, M., Neumann, E.-R., Davies, G.R., Timmerman, M.J., Heeremans, M., and Larsen, B.T.** (2004). Permo-Carboniferous magmatism and rifting in Europe: introduction, *Geol. Soc. Lond. Spec. Publ.*, 223, 1-10.
- Yiğitbaş, E., Kerrich, R., Yılmaz, Y., Elmas, A. & Xie, Q.** (2004). Characteristics and geochemistry of Precambrian ophiolites and related volcanics from the Istanbul-Zonguldak Unit, Northwestern Anatolia, Turkey: Following the missing chain of the Precambrian South European suture zone to the east. *Precambrian Res.*, 132, 179-206.

- Yılmaz, Y. & Tüysüz, O.** (1997). Geology and tectonic evolution of the Pontides. *Reg. Pet. Geol. Black Sea Surround. Reg. AAPG Mem.* 68.
- Yolsal-Çevikbilen, S. & Taymaz, T.** (2012). Earthquake source parameters along the Hellenic subduction zone and numerical simulations of historical tsunamis in the Eastern Mediterranean. *Tectonophysics.* 536-537, 61-100.
- Yoo, S.H., Rhie, J., Choi, H. & Mayeda, K.** (2011). Coda-derived source parameters of earthquakes and their scaling relationships in the Korean peninsula. *Bull. Seismol. Soc. Am.*, 101, 2388-2398.





CURRICULUM VITAE



Name Surname : Gizem İzgi
Place and Date of Birth : İzmir/ 15.04.1993
E-Mail : gizemzg@gmail.com

EDUCATION

- **B.Sc.** : 2017, Istanbul Technical University, Faculty of Mines, Geophysics Department
- **M.Sc.** : 2019, Istanbul Technical University, Faculty of Mines, Geophysics Department

PUBLICATIONS, PRESENTATIONS AND PATENTS ON THE THESIS:

- **Izgi, G., Eken, T., Gaebler, P. J., & Taymaz T.,** (2018). Frequency-Dependent Shear Wave Attenuation along the Western Part of the North Anatolian Fault Zone, EGU2018-629, Geophysical Research Abstracts, Vol. 20 | Oral | SM4.02. Fri, 13 Apr, 16:15–16:30, Room -2.2, EGU General Assembly 2018, 08-13 April 2018, Vienna, Austria
- **Izgi, G., Eken, T., Gaebler, P. J., & Taymaz T.,** (2018). Frequency-Dependent Shear Wave Attenuation along the Western Part of the North Anatolian Fault Zone, Special Session On Geoscientist of the Future, 71th Geological Congress of Turkey, 23-27 April 2018.

